

Comparison of Tokamak Linear Microstability Calculations between the Gyrokinetic Codes QuaLiKiz and GENE

Internship report by

Oliver Linder

At CEA Cadarache, IRFM

Supervisors:

Dr. Jonathan Citrin (FOM Institute DIFFER; CEA, IRFM)

Dr. Clarisse Bourdelle (CEA, IRFM)

September 2016

Acknowledgments

This work was carried out at the *Institut de Recherche sur la Fusion par confinement Magnétique* (IRFM), part of the *Commissariat à l'énergie atomique et aux énergies alternatives* (CEA), at the research site at Cadarache, France from April to June 2016 with support by the EUROfusion consortium and the FuseNet Association.

The author would like to thank their supervisors for the opportunity to investigate an interesting and relevant topic of present research. Guidance by J. Citrin regarding the practical work with the gyrokinetic codes QuaLiKiz and linear GENE proved valuable, enabling independent work on this project. Discussions with both J. Citrin and C. Bourdelle about the underlying theory, investigative approaches, and the results of this project and the their work were very fruitful. The author is thus very grateful to both J. Citrin and C. Bourdelle for their support throughout this project.

Additionally, the author would like to thank Y. Camenen (Aix-Marseille Université) for contributing results obtained with the gyrokinetic code GKW to this project, thus providing additional verification for the research question. The author is also thankful to H. Doerk (IPP Garching) and the GENE team for practical advice and support regarding the work with linear-GENE.

This work used resources of the *National Energy Research Scientific Computing Center* (NERSC). The author thanks F. Jenko (UCLA) for supporting this project.

Nomenclature

Symbol	Quantity	Definition
a	tokamak minor radius	
A	atomic mass number	
B	magnetic field	
c	sound velocity	
d	distance between rational surfaces	
e	elementary charge ¹	$1.602\,176\,565 \times 10^{-19} \text{ C}$
E	electric field	
f	particle distribution function	
	particle fraction	
k	wavenumber	
L_X	gradient length of quantity X	$-X/\nabla X$
m	particle mass	
	poloidal mode number	
n	particle density	
	toroidal mode number	
p	pressure	
q	electric charge	
	safety factor	
r	radial coordinate	
\mathbf{r}	position vector	
R	tokamak major radius	
s	magnetic shear	$r\nabla q/q$
T	temperature	
v	velocity	
w	mode width	
x	distance to rational surface	
Z	atomic number	
α	normalized pressure gradient	$-q^2 R \sum_s \beta_s \nabla p_s / p_s$
β	normalized pressure	$p / (B^2 / 2\mu_0)$
γ	instability growth rate	
Γ	particle flux	
δ	banana width	$q\rho\sqrt{R/r}$
δX	perturbation of quantity X	
Δ	Shafranov-shift	
ε	inverse aspect ratio	r/R
θ	poloidal angle	
ϑ	pitch angle	
μ_0	vacuum permeability ¹	$4\pi \times 10^{-7} \text{ N A}^{-2}$
ν	collision frequency	
ρ	cyclotron radius	mv_{\perp}/qB
	normalized toroidal flux coordinate	
τ	ion to electron temperature ratio	T_i/T_e
ϕ	electrostatic potential	
χ	phase	$\mathbf{kr} - \omega t$
φ	toroidal angle	
ω	frequency	

Subscript Abbreviations

Symbol	
c	cyclotron
curv	curvature
d	drift
e	electron
eff	effective
i	ion
p	passing
	poloidal
	proton
s	species
t	trapped
★	diamagnetic

Contents

1	Introduction	1
1.1	Motivation	1
1.2	Turbulence Modeling	1
1.3	Scope of This Work	2
2	Linear Gyrokinetic Theory	3
2.1	Instabilities in Tokamaks	3
2.2	The Linear Gyrokinetic Equation	6
2.2.1	Derivation of the Linear Gyrokinetic Equation	6
2.2.2	The Ballooning Transform	9
2.2.3	Influence of Resonances on the Development of Instabilities	9
2.2.3.1	Derivation of the Resonant Frequencies	10
2.2.3.2	Influence of the Drift Frequency	11
2.3	The Fluid Limit	12
2.3.1	Integration of the Linear Gyrokinetic Equation in Velocity Space	13
2.3.2	The Strongly Driven Linear Gyrokinetic Equation in the Fluid Limit	14
2.3.3	Obtaining the Instability Characteristics	15
3	Investigative Approach	17
3.1	Overview of the Gyrokinetic Codes Used	17
3.1.1	QuaLiKiz	17
3.1.2	GENE	18
3.2	Determination of the Regime of Discrepancy between both Codes	18
3.2.1	Comparison of the Instability Growth Rates	19
3.2.2	Comparison of the Eigenfunctions	21
3.3	Validation of Accuracy	21
3.4	Analysis of the JET Hybrid Scenario 75225	23
4	Comparison of Growth Rate Calculations with QuaLiKiz and GENE	25
4.1	Growth Rate Comparison	25
4.1.1	Threshold Values of the Instability	25
4.1.2	Growth Rates at a Fixed Ion Temperature Gradient	28
4.2	Eigenfunction Comparison	29
4.3	Discussion	32
4.4	The JET Hybrid Scenario 75225	33
5	Conclusion	39
	Bibliography	41

1 Introduction

1.1 Motivation

Since mankind began utilizing fossil fuels as a source of energy at the dawn of the Industrial Revolution more than two centuries ago, the consumption of fossil energy carriers and consequently the emission of greenhouse gases has skyrocketed.² Evidence for the set in of an anthropogenic climate change, linked to this development, have been reported repeatedly.³ Moreover, the global primary energy consumption is predicted to increase further within the upcoming decades,⁴ while at the same time the production of fossil fuels, especially of oil, is expected to reach its limit.⁵ Consequently, clean, reliable, inexhaustible, and inexpensive alternatives to fossil fuel based energy production are necessary to overcome these challenges.

One possibility is the utilization of nuclear fusion of the two hydrogen isotopes deuterium and tritium into the heavier element helium through the reaction⁶



This process releases around 10 million times as much energy as burning an equivalent amount of fossil fuels,⁷ without the production of greenhouse gases or long-lived radioactive waste. Moreover, the fuels required are readily available and virtually inexhaustible, potentially lasting for billions of years.⁷ Since additionally the cost of fusion generated electricity is expected to be comparable to renewable energy sources,⁶ fusion power is a promising alternative to fossil fuel based energy production. The viability of this concept has been investigated in torus-shaped fusion reactors called *tokamaks* since the 1960s, with prominent experiments such as ITER, JET, or TFTR.⁶

Yet, achieving the conditions necessary to maintain a self-sustaining reaction is not trivial as this requires heating the fuels to temperatures above 170 million K,⁷ as well as ensuring sufficient particle confinement for hydrogen nuclei to fuse and for produced helium nuclei to transfer excess energy to the plasma. However, violent magnetohydrodynamic (MHD) instabilities on spatial scales of the plasma dimensions, such as e.g. kink or sausage instabilities, can disrupt and consequently extinguish the plasma, wherefore these perturbations have to be avoided to sustain the fusion plasma.⁸ Moreover, even in the absence of large scale perturbations, increased transport from the core of the plasma to the reactor walls due to micro-instabilities significantly decreases confinement and hence energy production. Therefore, understanding and controlling the processes giving rise to turbulent transport are relevant for the viable operation of fusion reactors.

1.2 Turbulence Modeling

The theory of turbulent transport in tokamaks has been studied since the early 1960s, supported by the development of gyrokinetic codes based on the Boltzmann equation as a means to bridge theory and experiment.^{9,10} Due to progress in gyrokinetic theory, the development of sophisticated algorithms, and advances in computational technology, present day nonlinear gyrokinetic codes such as GS2, GYRO, GENE, or GKW are capable of correctly predicting energy, particle, and momentum fluxes in tokamaks in many regimes as compared to experimental results.¹⁰ However, a major limitation of these gyrokinetic codes is the computational time necessary to obtain fluxes in tokamak reactors, as the run time for flux prediction at a single time step is about 5×10^4 CPUh.^{9,11} A reduction can be achieved by evaluating the Boltzmann equation in the quasilinear approximation, resulting in computation times of roughly 500 CPUh for the quasilinear versions of codes

mentioned. Applying additional simplifications, e.g. focusing on electrostatic turbulences, computation times can be brought down to as low as 10 CPUs, such as in the case of the code QuaLiKiz.¹² Due to the reduced computational effort of quasilinear gyrokinetic codes, the calculation of temperature, density, and rotational profiles by evaluating fluxes at different radial positions over the duration of several confinement times is possible by embedding the quasilinear codes into an integrated framework. In the case of QuaLiKiz, profiles can be predicted on a small number of CPUs within a day.^{9,11}

Since a reduction in computation time is achieved by simplifying the original Boltzmann equation, extensive benchmarking of the quasilinear codes against each other, against full nonlinear codes, and against experimental data is vital to ensure validity of the calculations.¹⁰ As for the fast quasilinear code QuaLiKiz, results obtained were validated with more complete modeling, i.e. nonlinear GYRO¹³ and GS2,¹² in a broad parameter range.

1.3 Scope of This Work

During validation of the code QuaLiKiz against more complete modeling, significant deviations from the behavior predicted by both linear and nonlinear GENE have been reported for instability growth rate calculations at low values of $s - \alpha$ around the GA-standard case¹³ and for heat flux simulations for the DEMO1 scenario,¹⁴ with the magnetic shear $s = r\nabla q/q$ being the normalized gradient of the safety factor q and with α denoting the normalized pressure gradient $\alpha = -q^2 R \sum_s \beta_s \nabla \ln p_s$. As the operational regime of low magnetic shear and high normalized pressure gradient is intrinsic to hybrid scenarios, ramp-up and ramp-down phases, as well as to ITER and DEMO scenarios,^{13,15,16} QuaLiKiz can currently not be used reliably for these highly relevant conditions.

As the applicability of QuaLiKiz in an even broader parameter range is desirable due to the code's fast modeling capabilities, this work aims at understanding the reason for the observed discrepancy at low values of $s - \alpha$ and thus provides approaches to fix this issue. At first, the exact parameter range where disagreement occurs is mapped out by comparing calculations of the instability growth rate and the threshold ion temperature gradient between QuaLiKiz and linear GENE for ion temperature gradient dominated modes in the electrostatic case. In the obtained region, the variation of the electrostatic potential with the poloidal angle is compared for both codes used and their influence on the instability growth rate discussed.

The report is thus organized as follows. In Sec. 2, an introduction to instabilities in tokamak plasmas is given and the linear gyrokinetic equation used by QuaLiKiz presented. Terms relevant to this investigation due to the appearance of the magnetic shear or the normalized pressure gradient are discussed regarding their influence on the drive of instabilities. The following section, i.e. Sec. 3, covers the approach taken to determine the regime of discrepancy between QuaLiKiz and GENE. Furthermore, an overview of both gyrokinetic codes is presented and the accuracy of the results obtained discussed. The results of this investigation are presented and discussed in Sec. 4, followed by a conclusion of this work in Sec. 5.

2 Linear Gyrokinetic Theory

The transport of particles and momentum, as well as of both electron and ion heat in magnetized plasmas is greatly enhanced by the occurrence of micro-instabilities.¹⁷ To obtain a basic understanding of the underlying processes necessary to identify relevant instability mechanisms, an overview of instabilities is presented in Sec. 2.1. Using gyrokinetic theory, characteristics of these instabilities can be calculated, allowing the prediction of fluxes in experimental devices for a given set of plasma parameters. In Sec. 2.2, a linear gyrokinetic equation resembling the one used by the code QuaLiKiz is derived and terms relevant for this investigation analyzed. Limiting cases for the instabilities introduced in Sec. 2.1 are presented in Sec. 2.3, where the fluid limit of the linear gyrokinetic equation is described.

2.1 Instabilities in Tokamaks

Turbulent transport in tokamaks is driven by pressure gradients, resulting in fluctuations of the particle distribution functions and their respective moments, such as particle density, temperature, momentum, and flux. Since the electromagnetic fields are related to the moments of the particle distribution functions through Maxwell's equations, fluctuations occur additionally in the case of the electrostatic and the magnetic potential, giving rise to fluctuating $\mathbf{E} \times \mathbf{B}$ drift velocities for particles. Consequently, turbulent transport is caused by radial $\mathbf{E} \times \mathbf{B}$ drifts, i.e. electrostatic transport, as well as by enhanced diffusion across radial magnetic field fluctuations, i.e. magnetic transport. Fluctuations of the electrostatic potential dominate turbulent transport at low values of the normalized plasma pressure $\beta = p/p_B = p/(B^2/2\mu_0)$ as typically encountered in experiments, whereas transport due to magnetic fluctuations becomes important at high values of β .¹⁸

In the core plasma, two kinds of instability modes are primarily responsible for enhanced transport, namely the slab-type and the curvature-type instability, both of which arise in the presence of particle drift perpendicular to the particle's motion along the magnetic field lines.¹⁹ As opposed to the curvature-type instability, the development of slab modes is independent of the toroidal plasma geometry, i.e. the magnetic curvature, and thus also occurs at an infinite aspect ratio.^{9,20} Since here the diamagnetic frequency due to the pressure gradient is coupled to the transit frequency of particles parallel to the magnetic field lines,⁹ only passing particles are affected by slab modes.

As the name of the curvature-type instability suggests, this mode develops in the presence of a curved or inhomogeneous magnetic field ∇B , coupling the diamagnetic frequency to the ∇B - and curvature drift frequencies.⁹ The instability condition for curvature modes can be expressed as $\nabla p \cdot \nabla B > 0$,¹⁹ requiring the alignment of both the driving pressure gradient and the gradient of the magnetic field for an instability to develop. Consequently, curvature modes are found only at the low field side of a tokamak, where both gradients point inward. On the high field side however, pressure and magnetic gradient are oriented in opposite directions, fulfilling the stability condition and thus ensuring stability with respect to curvature modes.

The driving mechanism of the curvature-type instability can be illustrated by considering the influence of pressure fluctuations on the plasma behavior, as depicted in Fig. 2.1, where regions of higher pressure and lower pressure are shown in dark and light blue, respectively. In the presence of curved magnetic fields, ions and electrons are subjected to vertical drifts proportional to the plasma temperature in opposite directions, cf. Eq. (2.19). Consequently, the respective particle fluxes $\Gamma_d = n\mathbf{v} \propto nT$ are directly proportional to the plasma pressure. As the vertical fluxes of identical particles in both regions are therefore of different magnitude, charges accumulate at the

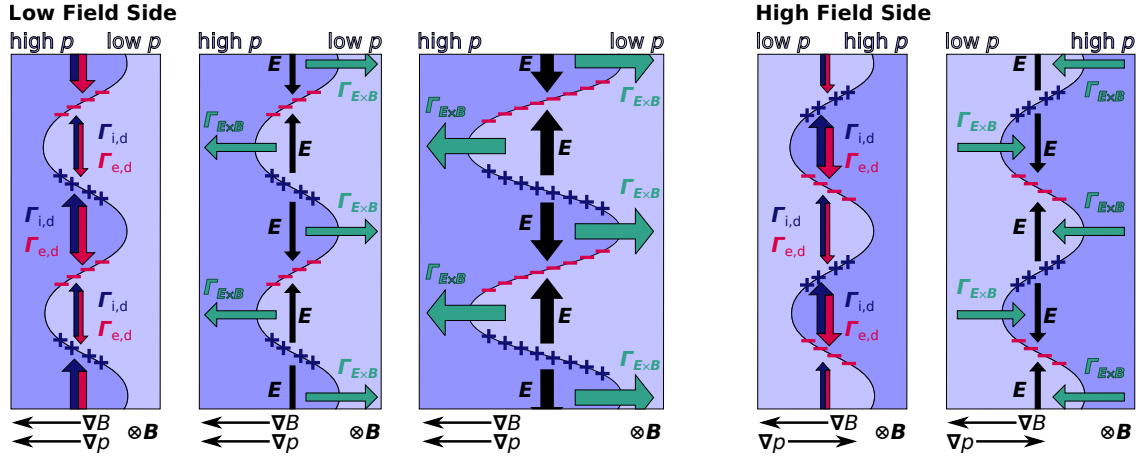


Fig. 2.1: The curvature-type instability develops in the presence of perturbations of the plasma pressure. The vertical particle drift Γ_d of ions and electrons due to the magnetic curvature is larger in the plasma regions of higher pressure as opposed regions of lower pressure, resulting in charge accumulation at the boundary (1st panel of the illustration) and consequently in the formation of electric fields \mathbf{E} (2. panel). On the low field side of the tokamak, the arising horizontal particle $\mathbf{E} \times \mathbf{B}$ -drifts transport particles from regions of higher pressure into regions of lower pressure and vice versa (2nd panel), increasing the boundary between both regions and consequently the accumulation of charges, thus reinforcing the initial perturbation (3rd panel). On the high field side however (4th panel), the $\mathbf{E} \times \mathbf{B}$ -drifts transport plasma of higher and lower pressure further into their respective regions (5th panel), decreasing the interjacent boundary and thus accumulation of charges, leading to a decay of the initial perturbation.

boundary between both regions, giving rise to electric fields. On the low field side of the tokamak, charge independent fluxes $\Gamma_{\mathbf{E} \times \mathbf{B}} = n \mathbf{E} \times \mathbf{B} / B^2$ due to $\mathbf{E} \times \mathbf{B}$ -drifts transport plasma of higher pressure into regions of lower pressure and vice versa, increasing the boundary between both regions. This in turn leads to further charge accumulation, reinforcing the initial perturbation of the plasma. Noticeably, the instability condition $\nabla p \cdot \nabla B > 0$ is verified in this case, as illustrated in Fig. 2.1. Following the same arguments, fluctuations at the high field side are stabilized by the arising $\mathbf{E} \times \mathbf{B}$ -drifts transporting plasma of higher and lower pressure further into the respective regions, decreasing the interjacent boundary, and thus the associated accumulation of charges. As a result, the initial perturbation is stabilized as stated by the stability condition. Therefore, the curvature-type instability can only develop on the low field side. However, since both sides are connected by poloidal magnetic fields, a strong parallel current stabilizes the instability as particles in their poloidal motion experience alternating regions of stability and instability.¹⁸ The connection length between low and high field side is determined by the ratio of toroidal to poloidal mode number, i.e. the safety factor q , increasing for larger values of q . Consequently, the curvature-type instabilities are more effective for high parallel resistivity and high values of the safety factor.¹⁹

For both the curvature-type and the slab-type instability, several branches of the particle population are potentially unstable, as listed in Table 2.1. Whereas only modes driven by passing particles can be of the slab-type instability, i.e. Ion Temperature Gradient modes (ITG) and Electron Temperature Gradient modes (ETG), all four branches can be of the curvature-type instability, including Trapped Ion Modes (TIM) and Trapped Electron Modes (TEM). The rotation of these modes is along the direction of the driving particles' diamagnetic drift and is thus different for ion and electron modes.¹⁷ For each branch, the characteristic wavelength is larger than or comparable to the characteristic length associated with the driving particle species, i.e. the cyclotron radius $\rho_c = mv_\perp / qB$ in the case of passing particles and the banana width $\delta \simeq q\rho \sqrt{R/r}$ for trapped particles, yielding the ordering $\delta_i > \rho_i > \delta_e > \rho_e$.²⁰ Expressed in terms of the ion cyclotron radius, the characteristic wavelengths for each branch are found as

$$\text{TIM:} \quad k_\theta \rho_i \lesssim 0.29$$

$$\text{ITG:} \quad k_\theta \rho_i \lesssim 1.0$$

$$\text{TEM:} \quad k_\theta \rho_i \lesssim 17$$

$$\text{ETG:} \quad k_\theta \rho_i \lesssim 60$$

Table 2.1: Potentially unstable branches of the particle population.^{18,20,21} Whereas all four branches can be of the curvature-type instability, only branches driven by passing particles can be of the slab-type instability. The characteristic wavelength is larger than or comparable to the driving particles' characteristic length, i.e. the cyclotron radius ρ_c or the banana width δ .

Mode Name	Driven By	Instability	Types	Characteristic Wavelength	
		Curvature	Slab		
Trapped Ion Mode (TIM):					
	trapped ions	X	-	$k_\theta \delta_i \lesssim 1.0$	$k_\theta \rho_i \lesssim 0.29$
Ion Temperature Gradient mode (ITG):					
	passing ions	X	X	$k_\theta \rho_i \lesssim 1.0$	$k_\theta \rho_i \lesssim 1.0$
Trapped Electron Mode (TEM):					
	trapped electrons	X	-	$k_\theta \delta_e \lesssim 1.0$	$k_\theta \rho_i \lesssim 17$
Electron Temperature Gradient mode (ETG):					
	passing electrons	X	X	$k_\theta \rho_e \lesssim 1.0$	$k_\theta \rho_i \lesssim 60$

for typical tokamak parameters. Thus, for a given wavelength of the instability, several branches might be unstable simultaneously. Note that TIMs are not relevant for increased transport since these modes are suppressed by nonlinear effects. cf. Refs. 22, 23.

The development of an instability depends on the magnitude of the governing temperature and density gradients, as illustrated exemplarily in Fig. 2.2 in the form of a stability diagram. Although quantitatively valid only for one choice of plasma parameters,⁹ these representations are suitable to demonstrate common behavior, cf. stability diagrams in Refs. 17, 20, 24. In the case of low gradients, no instability branch is unstable. However, above a critical threshold value of the normalized temperature gradient $-R\nabla T/T$ and the normalized density gradient $-R\nabla n/n$, electron or ion modes become unstable, giving rise to turbulent transport.^{17,18} The critical threshold above which instabilities set in is referred to as instability threshold throughout this work. Note that ion modes are primarily destabilized by temperature gradients, while the influence of density gradients is more significant for trapped electron modes, cf. Fig. 2.2. If particularly large gradients are present in the system, multiple modes can be unstable simultaneously. Hence, an separate treatment of modes is generally not possible.¹⁷

In the case of ion heat transport, the turbulence transport is primarily driven by ITG modes.²⁵ Since the turbulence is relatively weak, with fluctuations of the particle density in the order of a few percent,²⁵ linear calculations can capture the relevant behavior. Although ITG modes appear up to $k_\theta \rho_i \sim 1.0$, the most unstable wavenumbers are found between 0.1 and 0.3, dominating the turbulent ion heat transport.²⁵

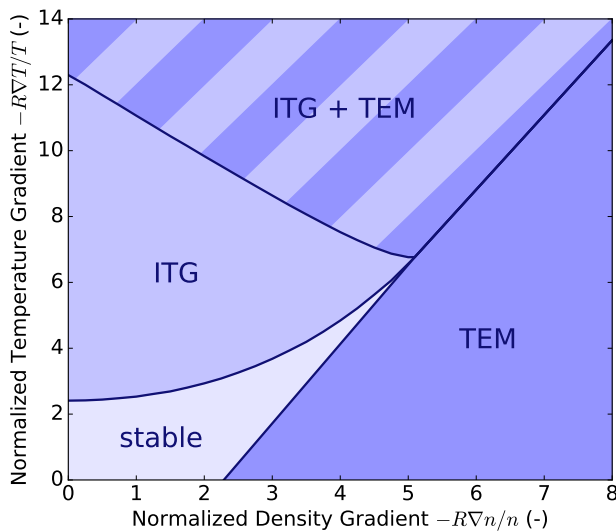


Fig. 2.2: Stability diagram for the potentially unstable branches listed in Table 2.1 for varying values of the normalized temperature gradient $-R\nabla T/T$ and the normalized density gradient $-R\nabla n/n$, adopted from Ref. 17. Although valid for only one choice of plasma parameters, these diagrams illustrate the threshold behavior of the instability branches below which no instabilities occur. For large gradients, multiple branches may be unstable simultaneously. Similar diagrams can be found in e.g. Refs. 20, 24.

2.2 The Linear Gyrokinetic Equation

Gyrokinetic theory is based on the evaluation of the Boltzmann-equation in the case of low frequencies ω of the perturbations, i.e. $\omega \ll \omega_c$ with ω_c being the particle cyclotron frequency. Since in this limit the characteristic time ω^{-1} associated with the evolution of the perturbative potential is significantly larger than the duration of one gyration period, the perturbations of the potentials can be averaged over the gyration orbit, hence the name *gyrokinetic equation*.^{10,26} The problem is thus reduced from 6 dimensions into a 5 dimensional problem, with three coordinates in position space, the parallel velocity, and the adiabatic invariant remaining, and is thus easier to solve.²⁷

In this section, a gyrokinetic equation resembling the one used by the code QuaLiKiz will be derived following the calculations by J. Weiland.²⁶ The approach presented is shorter and in some respect more comprehensible than other methods, such as e.g. a derivation using the formalism of angular and action variables, where the six dimensions of the problem are chosen as three conserved quantities and their associated frequencies, cf. e.g. Refs. 9, 21. Since QuaLiKiz works in the electrostatic limit, fluctuations of the magnetic potential will be neglected in the following analysis.

2.2.1 Derivation of the Linear Gyrokinetic Equation

The behavior of plasma particles can be described by particle distribution functions f , determined by the Boltzmann equation

$$\frac{df}{dt} = \frac{\partial f}{\partial t} + \dot{\mathbf{r}} \cdot \nabla_{\mathbf{r}} f + \ddot{\mathbf{r}} \cdot \nabla_{\dot{\mathbf{r}}} f = C(f_{s'}, f_s), \quad (2.1)$$

where the term $C(f_{s'}, f_s)$ accounts for collisions between species s' and s . In thermal equilibrium, the solution is given by a Maxwell-Boltzmann distribution

$$f_0 = n_0 \left(\frac{m}{2\pi T} \right)^{3/2} \exp \left(-\frac{m\mathbf{v}^2}{2T} \right) \quad (2.2)$$

for an equilibrium particle density n_0 . The particle distribution function f can be written as the sum of a background distribution $f_0(\mathbf{r}, \mathbf{v})$ and a small perturbation $\delta f(\mathbf{r}, \mathbf{v}, t) \ll f_0$, since density fluctuations in the plasma core are usually in the order of a few percents^{25,28} and are thus assumed to not affect the equilibrium Maxwellian distribution function f_0 .⁹ In high temperature fusion plasmas, collisions usually take place on time scales significantly larger than characteristic time scales of turbulent fluctuations.²⁷ Although collisions can often not be neglected, the behavior is still well described in the collisionless limit, wherefore the collisionless Boltzmann equation will be used, setting $C(f_{s'}, f_s) = 0$. Hence, the Vlasov equation describes both the equilibrium solution f_0 and the perturbation δf

$$\frac{df}{dt} = \frac{\partial}{\partial t} (f_0 + \delta f) + \mathbf{v} \cdot \nabla (f_0 + \delta f) + \frac{q}{m} (\delta \mathbf{E} + \mathbf{v} \times \mathbf{B}_0) \cdot \frac{\partial}{\partial \mathbf{v}} (f_0 + \delta f) = 0 \quad (2.3)$$

for a particle of charge q . Note that the electric field consists only of a perturbation $\delta \mathbf{E}$, whereas the magnetic field is not subjected to perturbations, corresponding to the electrostatic limit. Introducing cylindrical geometry for the velocity components with respect to the equilibrium magnetic field \mathbf{B}_0 , i.e.

$$\frac{\partial}{\partial \mathbf{v}} = \hat{\mathbf{e}}_{\perp} \frac{\partial}{\partial v_{\perp}} + \hat{\boldsymbol{\phi}} \frac{1}{v_{\perp}} \frac{\partial}{\partial \phi} + \hat{\mathbf{e}}_{\parallel} \frac{\partial}{\partial v_{\parallel}}, \quad (2.4)$$

the Vlasov equation for the general solution f can be expressed in zeroth order as

$$\mathbf{v} \cdot \nabla f_0 = \omega_c \frac{\partial f_0}{\partial \phi}. \quad (2.5)$$

Hence, for a gradient of the distribution function purely perpendicular to the magnetic field, the relation

$$\frac{\partial f_0}{\partial \mathbf{v}} = \frac{1}{\omega_c} \hat{\mathbf{e}}_{\parallel} \times \nabla f_0 + \hat{\mathbf{e}}_{\perp} \frac{\partial f_0}{\partial v_{\perp}} + \hat{\mathbf{e}}_{\parallel} \frac{\partial f_0}{\partial v_{\parallel}} \quad (2.6)$$

is obtained. Approximating the Vlasov equation of the total distribution function f in first order yields the expression

$$\frac{d\delta f}{dt} = -\frac{q}{m} \delta \mathbf{E} \cdot \frac{\partial f_0}{\partial \mathbf{v}}. \quad (2.7)$$

Integrating this equation and introducing Fourier harmonics, the perturbed distribution function can be written as²⁶

$$\delta f_k = -\frac{q}{m} \int_0^{\infty} \delta \mathbf{E}_k \frac{\partial f_0}{\partial \mathbf{v}} e^{-i[\mathbf{k}\mathbf{r}(\tau) - \omega\tau]} d\tau. \quad (2.8)$$

The phase $\chi(\tau) := \mathbf{k}\mathbf{r}(\tau) - \omega\tau$ includes a fast oscillating contribution due to the rapid gyration motion, as well as corrections to the frequency ω of the perturbation due to particle motion parallel to the magnetic field lines and due to particle drifts²⁶

$$\chi(\tau) = k_{\perp} \rho_c \sin(\omega_c \tau) - \int_0^{\tau} \underbrace{[\omega - k_{\parallel} v_{\parallel} - \mathbf{k}\mathbf{v}_d(t')]}_{=: \tilde{\omega}} dt'. \quad (2.9)$$

Replacing the electric field by a perturbative potential using $\delta \mathbf{E} = -\nabla \delta \phi$ and expressing the velocity derivative of the equilibrium distribution function in terms of Eq. (2.6), the integrand in Eq. (2.8) becomes

$$\left. \begin{aligned} \delta \mathbf{E}_k \frac{\partial f_0}{\partial \mathbf{v}} &= -i \frac{m}{T} \delta \phi_k \mathbf{k} \left[v_{\perp} \hat{\mathbf{e}}_{\perp} + v_{\parallel} \hat{\mathbf{e}}_{\parallel} - \underbrace{\frac{T}{m\omega_c} \hat{\mathbf{e}}_{\parallel} \times \frac{\nabla f_0}{f_0}}_{\equiv \mathbf{v}_{\star}} \right] f_0 \\ &= -i \frac{m}{T} f_0 [k_{\perp} v_{\perp} + k_{\parallel} v_{\parallel} - \omega_{\star}] \delta \phi_k. \end{aligned} \right\} \quad (2.10)$$

Note that the position space derivative ∇ transforms into $-i\mathbf{k}$ when using Fourier harmonics. In the expression obtained, the third term represents the diamagnetic drift frequency $\omega_{\star} := \mathbf{k} \cdot \mathbf{v}_{\star}$, with \mathbf{v}_{\star} being the diamagnetic drift velocity as defined in Eq. (2.10). As argued above, the equilibrium distribution function f_0 is assumed to be Maxwellian to calculate $\partial_{\mathbf{v}} f_0$. Since the first two terms of Eq. (2.10) appear in the temporal derivative of the exponential

$$\frac{d}{d\tau} e^{-i\chi(\tau)} = \frac{d}{d\tau} \exp(-i[\mathbf{k}\mathbf{r}(\tau) - \omega\tau]) = -i[k_{\perp} v_{\perp} + k_{\parallel} v_{\parallel} - \omega] e^{-i\chi(\tau)}, \quad (2.11)$$

the linearized Vlasov equation in Fourier representation can be reduced to

$$\delta f_k = \frac{q}{T} f_0 \left[1 + i(\omega - \omega_{\star}) \int_0^{\infty} e^{-i\chi(\tau)} d\tau \right] \delta \phi_k. \quad (2.12)$$

To evaluate the integral over the phase factor, the gyroperiod is assumed significantly smaller than other time scales involved. In this limit, the gyration motion is across a quasi-constant field, allowing the use of a gyroaveraged value $\langle \exp(-i\chi(\tau)) \rangle$ instead of the phase factor itself. Expressing the sine of the exponent as appearing in Eq. (2.9) as a series of Bessel functions, the gyroaveraged

value of the phase factor is found as

$$\begin{aligned}
\langle e^{-i\chi(\tau)} \rangle &= \int_{\tau}^{\tau+\Delta\tau} \exp \left(-i \left[k_{\perp} \rho_c \sin(\omega_c \tau) - \int_0^{\tau} \tilde{\omega} dt' \right] \right) d\tau \\
&= \int_{\tau}^{\tau+\Delta\tau} \sum_n J_n(k_{\perp} \rho_c) \exp \left(-in\omega_c \tau + i \int_0^{\tau} \tilde{\omega} dt' \right) d\tau \\
&\approx J_0(k_{\perp} \rho_c) \exp \left(i \int_0^{\tau} \tilde{\omega}(t') dt' \right)
\end{aligned} \tag{2.13}$$

The time interval $\Delta\tau$ is chosen to cover a relevant amount gyrations across the quasi-constant field while being much shorter than typical time steps of the system. Consequently, the integral vanishes in the limit $\Delta\tau \rightarrow 0$ and the series of Bessel functions can be approximated in zeroth order. As a result, the integral in the simplified Vlasov equation of Eq. (2.12) is replaced by an integral over the phase factor induced by corrections to the frequency ω of the perturbation. To evaluate this integral, the simplified Vlasov equation is differentiated with respect to the long time scale such that the Leibniz integral rule can be applied, yielding the linearized Vlasov equation

$$\delta f_k = \frac{q}{T} f_0 \left[1 - \frac{\omega - \omega_{\star}}{\omega - k_{\parallel} v_{\parallel} - \omega_d} J_0(k_{\perp} \rho_c) \right] \delta \phi_k. \tag{2.14}$$

This expression consists of an adiabatic term, followed by a non-adiabatic response. Instabilities are driven by the diamagnetic frequency ω_{\star} as this term incorporates deviations from the thermodynamical equilibrium through the presence of gradients of the equilibrium particle distribution function f_0 and consequently of the equilibrium temperature and density²⁹

$$\omega_{\star} = \mathbf{k} \cdot \frac{T}{m\omega_c} \hat{\mathbf{e}}_{\parallel} \times \frac{\nabla f_0}{f_0} = -\mathbf{k} \cdot \frac{T |\nabla n|}{m\omega_c n} (\hat{\mathbf{e}}_{\nabla} \times \hat{\mathbf{e}}_{\parallel}) \left[1 + \frac{L_n}{L_T} \left(\frac{mv^2}{2T} - \frac{3}{2} \right) \right]. \tag{2.15}$$

The effect of density and temperature gradients is incorporated in the respective gradient length $L_X := -X/\nabla X$. Resonances of the perturbation with the frequency $k_{\parallel} v_{\parallel}$ associated with the motion of the particles parallel to the magnetic field lines, as well as with the particle drift frequency ω_d influence the development of these gradient-driven instabilities.

The linearized Vlasov equation for one particle species is not sufficient to obtain the characteristics of the perturbation. For this purpose, the contributions of all particle species involved have to be coupled to Maxwell's equations, which in the electrostatic limit leads to the condition of quasineutrality, i.e. $\sum_s q_s n_s = 0$.^{9,21} Since in thermodynamic equilibrium, the densities of particles involved fulfill this condition, only density fluctuations have to be considered, which for each particle species are determined by a three-dimensional phase space integral of the linearized Vlasov equation, i.e. Eq. (2.14). To lighten notation, the abbreviation $\langle \dots \rangle \equiv \int \dots f_0/n_s d^3\mathbf{v}$ will be used. Hence, the condition of quasineutrality can be expressed as^{9,21}

$$\sum_s \frac{q_s^2 n_s}{T_s} \left[1 - f_p \left\langle \frac{\omega - \omega_{\star,s}}{\omega - k_{\parallel} v_{\parallel,s} - \omega_{d,s}} J_0(k_{\perp} \rho_{c,s}) \right\rangle_p - f_t \left\langle \frac{\omega - \omega_{\star,s}}{\omega - \omega_{d,s}} J_0(k_{\perp} \delta_s) \right\rangle_t \right] \delta \phi = 0, \tag{2.16}$$

where the summation considers all particle species present. This expression is the linear gyrokinetic equation determining the frequency ω , being the eigenvalue, and the shape of the electrostatic potential $\delta \phi$ of the perturbation, the eigenfunction. Passing and trapped particles, denoted by subscripts p and t respectively, are treated separately, as only the former have a finite averaged transit frequency $k_{\parallel} v_{\parallel,s}$, while the latter have an increased radius δ being the banana width due to their bouncing motion over which the quasiconstant perturbation is averaged. The fraction f of passing

and trapped particles depends on the inverse aspect ratio ϵ through the relation⁷ $f_t = \sqrt{2\epsilon/(1+\epsilon)}$ and $f_p = 1 - f_t$.

The expression presented in Eq.(2.16) describes the local dispersion relation, wherefore the integration is only over velocity space. To solve the linear gyrokinetic equation globally, QuaLiKiz uses a weak form of quasineutrality, i.e. $\int \sum_s q_s n_s \phi^* d^3\mathbf{r} = 0$, where the condition of quasineutrality is first multiplied by a test function chosen as the complex conjugate of the perturbed electrostatic potential and subsequently integrated over real space. Since the diamagnetic drift frequency ω_* , the transit frequency $k_{\parallel} v_{\parallel}$, the drift frequency ω_d , and the perturbed electrostatic potential $\delta\phi$ are spatially dependent, the only unknown left in the dispersion relation is the frequency ω of the instability. Since the shape of the eigenfunction $\delta\phi$ is assumed Gaussian, as discussed in Sec. 2.3.3, the dispersion relation is not solved fully self-consistently, thus allowing for a faster calculation. In the case of linear GENE however, the linear gyrokinetic equation is solved for each location along the field line such the shape of the perturbation $\delta\phi$ is consistent with the solution obtained. As linear GENE thus solves the linear gyrokinetic equation more self-consistently as compared to QuaLiKiz, the computational effort is significantly greater.

2.2.2 The Ballooning Transform

The calculation of the eigenvalues and the eigenfunctions of the linear gyrokinetic equation can be simplified by considering eigenfunctions which are localized around $\theta = 0$, i.e. strongly ballooned at the low field side, corresponding to the dominant curvature-type ITG modes.⁹ In this case, the potential for one poloidal harmonic can be expressed as³⁰

$$\phi_n^m(r) = \frac{1}{2\pi} \int_{-\pi}^{\pi} \phi_n(r, \theta) \exp(-im\theta + inq(r)\theta) d\theta, \quad (2.17)$$

where the poloidal and toroidal mode number are denoted by m and n , respectively. The envelope $\phi_n(r, \theta)$ is a slowly varying function of θ on the resonant field line as opposed to the exponential, the *eikonal*, which oscillates fast off the resonant surface.⁹ Since the eigenfunctions are typically confined to $\pm\pi$, the integration boundaries are set accordingly.⁹

Around the rational surface labeled by r_0 , the safety factor may be expanded in first order as $q(x) = q(0) + q'(0) \cdot x$, where $x := r - r_0$ denotes the distance to the rational surface of the mode. An expression for $q'(0)$ can be obtained by considering adjacent poloidal harmonics, yielding $q'(0) = 1/nd$ with d being the distance between rational surfaces. Using poloidal and toroidal angles, an alternative representation for the eikonal is given by $\exp(-in[\phi - q(0) \cdot \theta - q'(0) \cdot x\theta])$. Expressions for the components of the wave vector \mathbf{k} can be obtained by taking the respective derivatives of the eikonal:

$$\left. \begin{aligned} k_x \phi_n^m &= -i\partial_x \phi_n^m & \Rightarrow & k_x = nq'\theta = \frac{\theta}{d}, \\ k_{\theta} \phi_n^m &= -\frac{i}{r} \partial_{\theta} \phi_n^m & \Rightarrow & k_{\theta} = \frac{nq}{r} = \frac{nq'}{s}, \\ k_{\parallel} \phi_n^m &= -\frac{i}{R} \left(\partial_{\phi} + \frac{1}{q} \partial_{\theta} \right) \phi_n^m & \Rightarrow & k_{\parallel} \approx \frac{nq'x}{qR} = \frac{k_{\theta} s x}{qR}. \end{aligned} \right\} \quad (2.18)$$

Here, the magnetic shear $s = rq'/q$, describing the change of direction of the magnetic field,³¹ was introduced to simplify the expression for the parallel wavenumber. Above relations will be used in the following section to analyze particle transit and drift frequencies.

2.2.3 Influence of Resonances on the Development of Instabilities

The motion of charged particles parallel to the magnetic field lines, as well as their perpendicular drift due to the presence of inhomogeneous and curved magnetic fields influences the development of instabilities through resonances as can be seen from the linear gyrokinetic equation, cf.

Eq. (2.16). Since this contribution can strongly suppress the formation of turbulences, an expression for both the drift and the transit frequency will be derived in this section for a poloidal geometry in the presence of a shifted magnetic axis to analyze the effect of these frequencies on the stability of the system.

2.2.3.1 Derivation of the Resonant Frequencies

Charged particles in a curved or non-uniform magnetic field \mathbf{B} are subjected to a drift in a direction perpendicular to both the original magnetic field and the inhomogeneity with constant velocity

$$\mathbf{v}_d = \mathbf{v}_{\text{curv}} + \mathbf{v}_{\nabla B} = \frac{m}{qB} \left[v_{\parallel}^2 + \frac{v_{\perp}^2}{2} \right] \frac{\mathbf{B}}{B} \times \frac{\nabla B}{B}. \quad (2.19)$$

This expression is to be evaluated in a poloidal geometry where the magnetic axis and consequently the flux tubes are radially shifted. The magnetic geometry can thus be described by the following choice of coordinates

$$\tilde{R} = R + r \cos \theta + \Delta(r), \quad \tilde{Z} = r \sin \theta, \quad (2.20)$$

which are functions of the poloidal angle θ and the radial parameter r , ranging from 0 to the minor radius a . The radial shift $\Delta(r)$, referred to as Shafranov shift, is defined through the differential equation³¹

$$\Delta'(r) = \frac{2\mu_0}{rRB_{\theta}^2} \left[r^2 p - \int_0^r \left[2p + \frac{B_{\theta}^2}{2\mu_0} \right] r dr \right]. \quad (2.21)$$

and vanishes at the boundary of the plasma vessel, i.e. at $r = a$. From the definition of $\Delta(r)$, the second derivative is obtained as

$$\Delta''(r) = \frac{1}{R} \left[r\beta'_p - \beta_p + \frac{1}{2} \frac{2 \int_0^r B_{\theta}^2 r dr}{r^2 B_{\theta}^2} + \frac{4\mu_0 \int_0^r p r dr}{r^2 B_{\theta}^2} - 1 \right] = \frac{q^2}{\epsilon} \beta' - \frac{1}{R} \left[\beta_p - \frac{l_{\text{int}}}{2} - \bar{\beta}_p - 1 \right]. \quad (2.22)$$

The quantities l_{int} and $\bar{\beta}_p$ denote internal inductance and averaged poloidal normalized plasma pressure respectively. Introducing the normalized pressure gradient $\alpha = -q^2 R \beta'$, the second derivative of the Shafranov shift can be expressed in the form

$$\Delta''(r) = -\frac{1}{R} \left[\frac{\alpha}{\epsilon} + \beta_p - \bar{\beta}_p - \frac{l_{\text{int}}}{2} + 1 \right] \approx -\frac{\alpha}{\epsilon R}. \quad (2.23)$$

Considering the ordering in the inverse aspect ratio $\epsilon = r/R$ of the individual terms of this differential equation, the first term is of the order $\epsilon^{-1/2}$, since $\alpha \sim O(\epsilon^{1/2})$, whereas the remaining terms are of the order $O(1)$. Thus, in the limit of low inverse aspect ratios, i.e. $\epsilon \ll 1$, the second order differential equation can be approximated by above expression.

In the geometry introduced, the differential operator ∇ can be obtained from

$$ds^2 = d\tilde{R}^2 + d\tilde{Z}^2 = (1 + 2\Delta' \cos \theta) dr^2 + r^2 d\theta^2, \quad (2.24)$$

Consequently, the gradient is

$$\nabla = (1 + 2\Delta' \cos \theta)^{-1/2} \partial_r \hat{\mathbf{r}} + \frac{1}{r} \partial_{\theta} \hat{\boldsymbol{\theta}} \approx [1 + \alpha \cos \theta] \partial_r \hat{\mathbf{r}} + \frac{1}{r} \partial_{\theta} \hat{\boldsymbol{\theta}}. \quad (2.25)$$

Here, the initial expression of the gradient was simplified by an expansion in r up to first order, where the expression for Δ'' obtained in Eq. (2.23) as well as the boundary condition $\Delta'(0) = 0$ was used.

The total magnetic field can be approximated by the dominating toroidal component, yielding a radial dependence of

$$B = \frac{B_0}{1 + \frac{r}{R} \cos \theta + \frac{\Delta(r)}{R}} \approx B_0 \left[1 - \frac{r}{R} \cos \theta - \frac{r}{R} \Delta' \right] \quad (2.26)$$

for small values of the inverse aspect ratio. With these considerations, the gradient of the magnetic field can be written as

$$\frac{\nabla B}{B} = -\frac{1}{R} \left[[\cos \theta - \alpha \sin^2 \theta] \hat{\mathbf{r}} - \sin \theta \hat{\boldsymbol{\theta}} \right] \left[1 + \frac{r}{R} \cos \theta + \frac{\Delta}{R} \right], \quad (2.27)$$

where terms of order $O(\varepsilon)$ were neglected. Consequently, the vector product in the expression for the drift velocity, cf. Eq. (2.19), for $\mathbf{B}/B \approx \hat{\boldsymbol{\phi}}$ is

$$\frac{\mathbf{B}}{B} \times \frac{\nabla B}{B} = -\frac{1}{R} \left[\sin \theta \hat{\mathbf{r}} + [\cos \theta - \alpha \sin^2 \theta] \hat{\boldsymbol{\theta}} \right] \left[1 + \frac{r}{R} \cos \theta + \frac{\Delta}{R} \right]. \quad (2.28)$$

From this expression, the drift velocity \tilde{v}_d is readily obtained as

$$\tilde{v}_d = -\frac{m}{qBR} \left[v_{\parallel}^2 + \frac{v_{\perp}^2}{2} \right] \left[1 + \frac{r}{R} \cos \theta + \frac{\Delta}{R} \right] \quad (2.29)$$

with its components being

$$v_{d,r} = \tilde{v}_d \sin \theta, \quad v_{d,\theta} = \tilde{v}_d [\cos \theta - \alpha \sin^2 \theta]. \quad (2.30)$$

Note that the terms $r/R \cdot \cos \theta + \Delta/R$ are of the order $O(\varepsilon)$ and are thus omitted in QuaLiKiz. Nevertheless, the respective terms are considered in the following derivations for the sake of completeness.

To obtain the drift and transit frequency, the Doppler shift in the eikonal has to be considered. Since the modes are proportional to $\exp(-i n [\varphi - q\theta] - i \omega t)$, the change in phase $n\chi = n [\varphi - q\theta]$ is

$$\begin{aligned} n\dot{\chi} &= n [\dot{\varphi} - q\dot{\theta} - q\dot{\theta}] = \frac{nv_{\parallel}}{R} - n \frac{dq}{dr} \frac{dr}{dt} \theta - nq \left[\frac{v_{\parallel}}{qR} + \frac{v_{d,\theta}}{r} \right] \\ &\approx -\frac{nq'x}{qR} v_{\parallel} - nq' \tilde{v}_d \theta \sin \theta - \frac{nq\tilde{v}_d}{r} [\cos \theta - \alpha \sin^2 \theta]. \end{aligned} \quad (2.31)$$

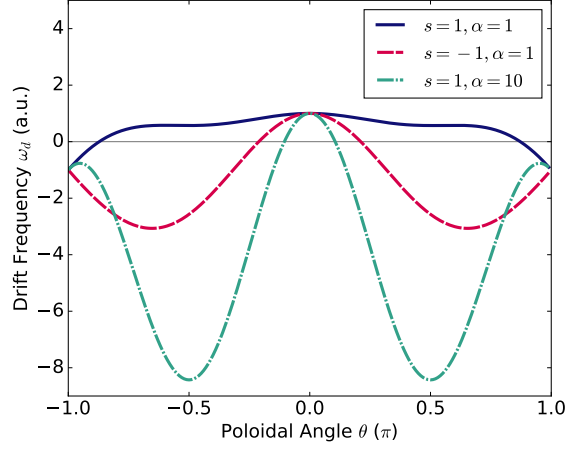
Using the expressions for the components of the wavevector \mathbf{k} introduced in Eqs. (2.18) for further simplification, the transit and drift frequencies are found as

$$k_{\parallel} v_{\parallel} = \frac{k_{\theta} s x}{qR} v_{\parallel}, \quad \omega_d = k_{\theta} \tilde{v}_d [\cos \theta + [s\theta - \alpha \sin \theta] \sin \theta]. \quad (2.32)$$

2.2.3.2 Influence of the Drift Frequency

The development of instabilities is strongly influenced by the drift frequency ω_d , as the drive of instabilities can be suppressed by negative drift frequencies. Being a function of the magnetic shear s and the normalized pressure gradient α , cf. Eq. (2.32), the drift frequency is positive throughout a major part of the poloidal cross section and negative only at the very high field side in the case of moderate values of both parameters. However, for low values of the magnetic shear or large values of α , the drift frequency is of negative sign throughout a large part of the poloidal cross section, as illustrated in Fig. 2.3 for three different combinations of both parameters. An increase

Fig. 2.3: Influence of the magnetic shear s and the normalized pressure gradient α on the drift frequency ω_d , cf. Eq. (2.32), in arbitrary units as function of the poloidal angle θ . For low values of s (red line) or large values of α (green line), the drift frequency is of negative sign for most poloidal angles and positive only at the very low field side, whereas the reference case (blue line) is only negative at the very high field side.



of the normalized pressure gradient $\alpha = -q^2 \beta R \nabla p / p$ is more effective to achieve negative drift frequencies as opposed to a reduction of the magnetic shear $s = r \nabla q / q$, i.e. the formation of a flat or a reversed profile of the safety factor q . Note that even though instabilities are driven by pressure gradients, the reduction in curvature and ∇B -drifts through α -stabilization outweighs the $|\nabla p|/p$ -destabilization above a certain threshold.³²

By achieving negative drift frequencies, the drive of the curvature-type instabilities is suppressed. In the fluid-limit, the growth rate γ of curvature modes is proportional to the square root of the drift frequency, i.e. $\gamma^2 \propto \omega_d \omega_*$, as will be shown in Sec. 2.3 (cf. Eq. (2.55)). Hence, for negative values of the drift frequency, the instability growing with $\exp(\gamma t)$ is stabilized with γ becoming imaginary, causing an oscillation rather than an exponential growth. Since stabilization is due to choices of the magnetic shear and the normalized pressure gradient, this mechanism is referred to as s - α -stabilization.

2.3 The Fluid Limit

The linear gyrokinetic equation introduced in Sec. 2.2 (cf. Eq. (2.16)) allows the calculation of instability characteristics such as the driving frequency ω and the growth rate $\gamma = \Im(\omega)$ for arbitrary plasma parameters. However, by analyzing the linear gyrokinetic equation in the strongly driven case, the dependence of the instability characteristics on the individual factors of the linear gyrokinetic equation far from the instability threshold can be investigated and dominant branches identified. As instabilities approach this limit in the case of strong gradients, an analytic solution will be presented, following the derivation by C. Bourdelle.²¹

In the fluid limit, the plasma is considered to be strongly driven such that the driving frequency ω is significantly larger than particle transit frequency $k_{\parallel} v_{\parallel}$ and particle drift frequency ω_d . Consequently, the non-adiabatic response of one particle species s can be expressed as a series up to first order in ω_d and second order in $k_{\parallel} v_{\parallel}$, yielding

$$\frac{\omega - \omega_{*,s}}{\omega - k_{\parallel} v_{\parallel,s} - \omega_{d,s}} \approx \left(1 - \frac{\omega_{*,s}}{\omega}\right) \left[1 + \frac{k_{\parallel} v_{\parallel,s}}{\omega} + \frac{\omega_{d,s}}{\omega} + \left(\frac{k_{\parallel} v_{\parallel,s}}{\omega}\right)^2\right], \quad (2.33)$$

where mixed terms have been neglected. Since the characteristic length of the particle species involved is usually much smaller than the wavelength of the instability, the series defining the zeroth order Bessel function used in the linear gyrokinetic equation (cf. Eq. (2.16)) may be terminated after the second term for small arguments $k_{\perp} \rho_s$, such that $J_0(k_{\perp} \rho_s) \approx 1 - k_{\perp}^2 \rho_s^2 / 4$. As both the gyroradius ρ_e and the banana width δ_e of electrons are much smaller than the ion cyclotron radius ρ_i , the averaging of the perturbing potential due to the electrons' gyration motion is negligible and the series representing the Bessel function in the respective integrals can be terminated after the first term. Moreover, passing electrons can be assumed to be very adiabatic such that the transit

frequency dominates over the instability driving frequency, resulting in the non-adiabatic part to vanish. Applying these approximations to the linear gyrokinetic equation yields the expression

$$\begin{aligned} & \left[\frac{n_e}{T_e} \left[1 - \left\langle 1 - \frac{\omega_{*,e}}{\omega} + \frac{\omega_{d,e}}{\omega} \left(1 - \frac{\omega_{*,e}}{\omega} \right) \right\rangle_t \right] + \sum_i \frac{n_i Z_i^2}{T_i} \left[1 + \right. \\ & - \left\langle 1 - \frac{\omega_{*,i}}{\omega} + \frac{k_{\parallel} v_{\parallel,i}}{\omega} \left(1 - \frac{\omega_{*,i}}{\omega} \right) + \frac{\omega_{d,i}}{\omega} \left(1 - \frac{\omega_{*,i}}{\omega} \right) + \left(\frac{k_{\parallel} v_{\parallel,i}}{\omega} \right)^2 \left(1 - \frac{\omega_{*,i}}{\omega} \right) - \frac{k_{\perp}^2 \rho_i^2}{4} \left(1 - \frac{\omega_{*,i}}{\omega} \right) \right\rangle_p \\ & \left. - \left\langle 1 - \frac{\omega_{*,i}}{\omega} + \frac{\omega_{d,i}}{\omega} \left(1 - \frac{\omega_{*,i}}{\omega} \right) - \frac{k_{\perp}^2 \delta_i^2}{4} \left(1 - \frac{\omega_{*,i}}{\omega} \right) \right\rangle_t \right] \delta\phi = 0. \end{aligned} \quad (2.34)$$

The summation over i considers all ion species present in the system. Note that mixed terms of the characteristic lengths with other than the diamagnetic drift frequency $\omega_{*,i}$ have been neglected.

2.3.1 Integration of the Linear Gyrokinetic Equation in Velocity Space

As compared to the linear gyrokinetic equation of Eq. (2.16), the factors f denoting the fractions of passing or trapped particles were dropped in the strongly driven linear gyrokinetic equation, cf. Eq. (2.34). Hence, the boundaries for integration over velocity space in spherical coordinates (v, ϑ, φ) have to be adjusted accordingly for each particle species. Assuming a Maxwellian particle velocity distribution, if the perpendicular velocity component v_{\perp} of a particle satisfies the condition $v_{\perp} > v \sin \vartheta_p$, the particle is trapped between the tokamak's high field side and its low field side, as illustrated in Fig. 2.4. Complementary, particles with a small perpendicular velocity $v_{\perp} < v \sin \vartheta_p$ are free to move along the tokamak's toroidal direction, hence they are passing particles. The angle ϑ_p separating passing from trapped particles is determined by the ratio between the magnetic field B_{\min} at the low field side and the magnetic field B_{\max} at the high field side via $\sin^2 \vartheta_p = B_{\min}/B_{\max}$, cf. Ref. 7. Using the magnetic geometry introduced in Sec. 2.2.3, the magnetic field at both the low and high field side can be related to the inverse aspect ratio $\varepsilon = r/R$, yielding the relation $\sin^2 \vartheta_p = (1 - \varepsilon)/(1 + \varepsilon)$.

Having defined the passing particle angle ϑ_p , integration over the pitch angle ϑ is performed in the range $\vartheta \in [\vartheta_p, \pi - \vartheta_p]$ for trapped particles and in the region $\vartheta \in [0, \vartheta_p] \cup [\pi - \vartheta_p, \pi]$ in the case of passing particles, cf. Fig. 2.4. Consequently, the velocity space integral in spherical coordinates for an arbitrary function $f(v, \vartheta) = F(v) \cdot G(\vartheta)$ can be written as

$$\begin{aligned} & \int_0^{\infty} \int_0^{2\pi} \int_{\vartheta} F(v) G(\vartheta) \frac{f_0}{n_0} v^2 \sin \vartheta dv d\varphi d\vartheta = \left(\frac{m^3}{2\pi T^3} \right)^{1/2} \int_0^{\infty} v^2 F(v) \exp \left(-\frac{mv^2}{2T} \right) dv \int_{\vartheta} \sin \vartheta G(\vartheta) d\vartheta \\ & = \langle F(v) \rangle \langle G(\vartheta) \rangle_{p,t}. \end{aligned} \quad (2.35)$$

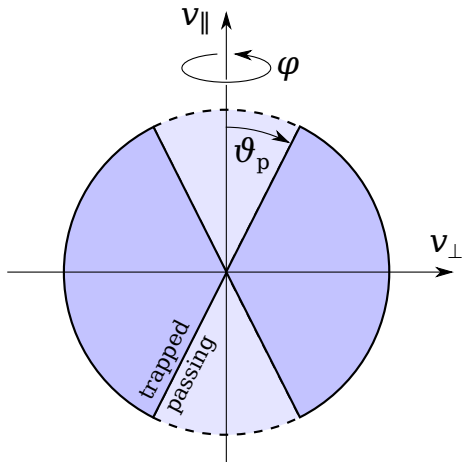


Fig. 2.4: Velocity space of an isotropic Maxwellian distribution. Particles with a perpendicular velocity component $v_{\perp} > v \sin \vartheta_p$ are trapped between high field side and low field side of the tokamak, whereas particles with $v_{\perp} < v \sin \vartheta_p$ can move freely along the toroidal direction.

To evaluate the expression for the strongly driven linear gyrokinetic equation, cf. Eq. (2.34), the following moments $\langle F(v) \rangle$ of the velocity integral are required:

$$\langle 1 \rangle = \frac{1}{2}, \quad \langle v^2 \rangle = \frac{3T}{2m}, \quad \langle v^4 \rangle = \frac{15T^2}{2m^2}. \quad (2.36)$$

An expression for the fraction of trapped and passing particles can be obtained by taking the respective zeroth order moments of the pitch angle integration, i.e.

$$\langle 1 \rangle_t = 2 \left(\frac{2\varepsilon}{1+\varepsilon} \right)^{1/2}, \quad \langle 1 \rangle_p = 2 \left[1 - \left(\frac{2\varepsilon}{1+\varepsilon} \right)^{1/2} \right]. \quad (2.37)$$

Hence, the fractions of passing and trapped particles are found as

$$f_t = \langle 1 \rangle \langle 1 \rangle_t = \left(\frac{2\varepsilon}{1+\varepsilon} \right)^{1/2}, \quad f_p = \langle 1 \rangle \langle 1 \rangle_p = 1 - \left(\frac{2\varepsilon}{1+\varepsilon} \right)^{1/2} = 1 - f_t, \quad (2.38)$$

in agreement with the expressions introduced in Sec. 2.2.1. Additionally, the following moments of the θ -integration are necessary:

$$\left. \begin{aligned} \langle \cos \vartheta \rangle_p &= 0, \quad \langle \cos^2 \vartheta \rangle_p = 2 \left[f_p - f_p^2 + \frac{f_p^3}{3} \right] \approx \frac{2}{3} f_p, \quad \langle \sin^2 \vartheta \rangle_p = \frac{2}{3} [f_p^2 - f_p^3] \approx 0, \\ \langle \cos^2 \vartheta \rangle_t &= \frac{2}{3} f_t^3 \approx 0, \quad \langle \sin^2 \vartheta \rangle_t = 2f_t - \frac{2}{3} f_t^3 \approx 2f_t. \end{aligned} \right\} \quad (2.39)$$

2.3.2 The Strongly Driven Linear Gyrokinetic Equation in the Fluid Limit

For further analysis the moments introduced in Eqs. (2.36) and (2.39) are used in linear approximation in the respective fraction f of passing or trapped particles. With these considerations made, the integration of the individual terms of the strongly driven linear gyrokinetic equation is straightforward, but necessitates the redefinition of several quantities using the moments of the velocity integration introduced in Eqs. (2.36). Integration of the diamagnetic drift frequency terms yields a dependence on only density gradients for pure terms in ω_* and a dependence on the pressure gradient for mixed terms in ω_* :

$$\omega_{*,s}^n = -\mathbf{k} \cdot \frac{T}{q_s B L_n} (\hat{\mathbf{e}}_{\nabla} \times \hat{\mathbf{e}}_{\parallel}), \quad \omega_{*,s}^p = \omega_{*,s}^n \left[1 + \frac{L_n}{L_T} \right]. \quad (2.40)$$

For the drift frequency ω_d , the squared transit frequency $k_{\parallel}^2 v_{\parallel}^2$, and the banana width δ , the following expressions are obtained:

$$\left. \begin{aligned} \omega_{d,s}^t &= -\frac{3}{2} k_{\theta} \frac{T}{q_s B R} \left[1 + \frac{r}{R} \cos \theta + \frac{\Delta}{R} \right] [\cos \theta + [s \theta - \alpha \sin \theta] \sin \theta], \\ \omega_{d,s}^p &= 2 \omega_{d,s}^t, \quad (k_{\parallel} v_{\parallel,s})^2 = 2 k_{\parallel}^2 \frac{T}{m}, \quad \delta^2 = 3 \frac{q^2}{\varepsilon} \frac{T}{m \omega_{c,s}^2}. \end{aligned} \right\} \quad (2.41)$$

Consequently, the strongly driven linear gyrokinetic equation can be written in the fluid limit as

$$\left. \begin{aligned} & \left[\frac{n_e}{T_e} \left[1 - f_t \left[1 - \frac{\omega_{*,e}^n}{\omega} + \frac{\omega_{d,e}^t}{\omega} \left(1 - \frac{\omega_{*,e}^p}{\omega} \right) \right] \right] + \sum_i \frac{n_i Z_i^2}{T_i} \left[1 + \right. \right. \\ & - f_p \left[1 - \frac{\omega_{*,i}^n}{\omega} + \frac{\omega_{d,i}^p}{\omega} \left(1 - \frac{\omega_{*,i}^p}{\omega} \right) + \frac{k_{\parallel}^2 v_{\parallel}^2}{\omega^2} \left(1 - \frac{\omega_{*,i}^p}{\omega} \right) \right] + \\ & \left. \left. - f_t \left[1 - \frac{\omega_{*,i}^n}{\omega} + \frac{\omega_{d,i}^t}{\omega} \left(1 - \frac{\omega_{*,i}^p}{\omega} \right) - \frac{k_{\perp}^2 \delta^2}{4} \left(1 - \frac{\omega_{*,i}^p}{\omega} \right) \right] \right] \right] \delta \phi = 0. \end{aligned} \right\} \quad (2.42)$$

Note that the finite Larmor radius effect for passing particles vanishes as the perpendicular velocity component equals zero in first order in the passing particle fraction f_p . Additionally, the linear term of the ion transit frequency disappears as the parallel velocity has no preferred direction in the case of an isotropic Maxwellian velocity distribution. The expression obtained can be simplified further by using the following relations, with the ion temperature expressed in terms of the electron temperature, i.e. $T_i = \tau T_e$, and the ion atomic number Z_i approximated by half the ion's atomic mass number A_i , i.e. $Z_i = A_i/2$:

$$\sum_i \frac{n_i Z_i^2}{T_i} v_{\parallel,i}^2 = \frac{n_e}{T_e} c_{\text{eff}}^2 \quad \text{with} \quad c_{\text{eff}}^2 = \frac{T_e}{2m_p}, \quad (2.43)$$

$$\sum_i \frac{n_i Z_i^2}{T_i} v_{\parallel,i}^2 \omega_{*,i}^p = \frac{n_e}{T_e} \frac{\tau}{\bar{Z}} c_{\text{eff}}^2 \omega_{*,e}^p, \quad (2.44)$$

$$\sum_i \frac{n_i Z_i^2}{T_i} \delta_i^2 = \frac{n_e}{T_e} \delta_{\text{eff}}^2, \quad (2.45)$$

$$\sum_i \frac{n_i Z_i^2}{T_i} \delta_i^2 \omega_{*,i}^p = -\frac{n_e}{T_e} \frac{\tau}{\bar{Z}} \delta_{\text{eff}}^2 \omega_{*,e}^p, \quad (2.46)$$

$$\sum_i \frac{n_i Z_i^2}{T_i} \omega_{*,i}^n = -\frac{n_e}{T_e} \omega_{*,e}^n, \quad (2.47)$$

$$\sum_i \frac{n_i Z_i^2}{T_i} (f_p \omega_{d,i}^p + f_t \omega_{d,i}^t) = -\frac{n_e}{T_e} (f_p \omega_{d,e}^p + f_t \omega_{d,e}^t), \quad (2.48)$$

$$\sum_i \frac{n_i Z_i^2}{T_i} \left(\frac{f}{p} \omega_{d,i}^p \omega_{*,i}^p + \frac{f}{t} \omega_{d,i}^t \omega_{*,i}^p \right) = \frac{n_e}{T_e} \frac{\tau}{\bar{Z}} \gamma_{\text{eff}}^2 \quad \text{with} \quad \gamma_{\text{eff}}^2 = f_p \omega_{d,e}^p \omega_{*,e}^p + f_t \omega_{d,e}^t \omega_{*,e}^p. \quad (2.49)$$

With the quantity $1/\bar{Z}$ defined as $1/\bar{Z} = \sum_i n_i L_{p,e}/n_e L_{p,i}$, the expression τ/\bar{Z} denotes the ratio of ion to electron pressure gradient, i.e. $\tau/\bar{Z} = \sum_i \nabla p_i / \nabla p_e$. Substituting the respective terms in Eq. (2.42) with above expressions, the relation

$$\left[1 + \frac{f_t \omega_{*,e}^p \omega_{d,e}^t + \frac{\tau}{\bar{Z}} \gamma_{\text{eff}}^2}{f_p \omega^2} - \frac{\omega_{*,e}^n}{\omega} + \frac{\omega_{d,e}^p}{\omega} + \left(-\frac{k_{\parallel}^2 c_{\text{eff}}^2}{\omega^2} + \frac{f_t}{f_p} \frac{k_{\perp}^2 \delta_{\text{eff}}^2}{4} \right) \left(1 + \frac{\tau}{\bar{Z}} \frac{\omega_{*,e}^p}{\omega} \right) \right] \delta\phi = 0 \quad (2.50)$$

is found for the fluid form of the strongly driven linear gyrokinetic equation.

2.3.3 Obtaining the Instability Characteristics

Making the assumption that the width w of the modes of the perturbed potential is significantly smaller than the magnetic shear length $L_q = q/\nabla q$, the parallel component of the wave vector can be approximated as $k_{\parallel} = \nabla k_{\parallel} \cdot \partial_{k_r}$, with the radial component related to the other components by $k_{\perp}^2 = k_{\theta}^2 + k_r^2$. Replacing the factors including the radial component by the expressions $k_r \rightarrow -i\partial_x$ and $\partial_{k_r} \rightarrow x$ as used in the ballooning transform (cf. Eqs. (2.18)), above equation, i.e. Eq. (2.50), becomes a second order differential equation. Using a Gaussian ansatz $\delta\phi = \phi_0 \exp(-x^2/2w^2)$ for the perturbed potential, the differential equation to be solved is found as

$$\frac{\partial^2}{\partial x^2} \delta\phi = \left[-\frac{1}{w^2} + \frac{1}{w^4} x^2 \right] \delta\phi. \quad (2.51)$$

By comparing the individual terms of this differential equation with the simplified fluid form of the strongly driven linear gyrokinetic equation, i.e. Eq. (2.50), both the mode with w and the growth rate $\gamma = \Im(\omega)$ of the mode can be determined. Analyzing the terms proportional to x^2 , the relation

$$w^2 = i \frac{\omega \delta_{\text{eff}}}{2 |\nabla k_{\parallel}| c_{\text{eff}}} \left(\frac{f_t}{f_p} \right)^{1/2} \quad (2.52)$$

is obtained. Note that the spatial derivative of the parallel component of the wave vector can be written as $\nabla k_{\parallel} = k_{\theta}/L_q$. Substituting the mode width in the constant term of the differential equation with above expression, the second order polynomial

$$\left. \begin{aligned} & \omega^2 \left[1 + \frac{k_{\theta}^2 \delta_{\text{eff}}^2}{4} \frac{f_t}{f_p} \right] + \omega \left[-\omega_{*,e}^n + \omega_{d,e}^p + \frac{\mathbf{i}}{2} c_{\text{eff}} \delta_{\text{eff}} \frac{k_{\theta}}{L_q} \left(\frac{f_t}{f_p} \right)^{1/2} + \frac{\tau}{\bar{Z}} \omega_{*,e}^p \frac{k_{\theta}^2 \delta_{\text{eff}}^2}{4} \frac{f_t}{f_p} \right] + \\ & + \frac{\mathbf{i}}{2} c_{\text{eff}} \delta_{\text{eff}} \frac{\tau}{\bar{Z}} \omega_{*,e}^p \frac{k_{\theta}}{L_q} \left(\frac{f_t}{f_p} \right)^{1/2} + \frac{f_t \omega_{d,e}^l \omega_{*,e}^p + \frac{\tau}{\bar{Z}} \gamma_{\text{eff}}^2}{f_p} = 0 \end{aligned} \right\} \quad (2.53)$$

in the perturbation frequency ω has to be solved to find the growth rate of the instability.

In the case of curvature-type instabilities, the finite Larmor radius effect can be neglected, setting $\delta_{\text{eff}} = 0$. Furthermore, in this limit the pressure gradient is dominated by the temperature gradient such that $L_{n,e} \gg L_{T,e} \approx L_{p,e}$. Here, the pressure gradient length is still smaller than the characteristic size R of the machine. Consequently, the ordering

$$\omega_{*,e}^n{}^2 \propto L_{n,e}^{-2} < \omega_{d,e}^2 \propto R^{-2} < \omega_{d,e} \omega_{*,e}^p \propto R^{-1} L_{T,e}^{-1} \quad (2.54)$$

is obtained for the remaining terms (cf. Eqs. (2.40) and (2.41)). Assuming strongly trapped particles, the drift frequency of both passing and trapped electrons can be described by a single frequency $\omega_{d,e}$. Applying these considerations to the second order polynomial described above, the growth rate of the curvature-type instability is found as

$$\left. \begin{aligned} \gamma &= \left(\omega_{d,e} \omega_{*,e}^p \frac{f_t + \frac{\tau}{\bar{Z}}}{f_p} \right)^{1/2} \\ &= k_{\theta} \frac{T}{q_s B} \left(\frac{3}{2} \frac{1}{L_T R} \left[1 + \frac{r}{R} \cos \theta + \frac{\Delta}{R} \right] [\cos \theta + [s \theta - \alpha \sin \theta] \sin \theta] \right)^{1/2}. \end{aligned} \right\} \quad (2.55)$$

In this limit, instabilities are driven entirely by temperature gradients $1/L_T = -\nabla T/T$, with the growth rate of the instability increasing as the square root of the gradient $\gamma \propto \sqrt{1/L_T}$. Note that this result is valid only in the presence of low density gradients and for low inverse aspect ratios. Moreover, as argued before, for low values of the magnetic shear s and high values of the normalized pressure gradient α , the growth rates becomes imaginary, suppressing instabilities.

3 Investigative Approach

In a comparison of instability growth rates as calculated by the quasilinear code QuaLiKiz with both linear and nonlinear GENE results in the limit of low magnetic shear, major differences have been observed, as outlined in the introduction of this work, cf. Sec. 1. The stabilization of the instabilities due to a decrease in the magnetic shear s was reported to be overestimated as compared to calculations by GENE.¹³ Similarly, an increase of the normalized pressure gradient α was also found to result in an overestimation of the stabilizing impact of this parameter.¹⁴ As this regime is relevant for hybrid scenarios in present day devices, the operation of future machines, as well as for ramp-up and ramp-down phases, this issue of overestimation of stabilizing mechanisms by QuaLiKiz has to be resolved to enable reliable use of QuaLiKiz in these cases. For this purpose, the instability growth rate γ in the parameter range of low magnetic shear and high values of the α -parameter is to be mapped out using QuaLiKiz and linear-GENE. Furthermore, the eigenfunctions obtained from both codes are compared in the parameter regime investigated to analyze the validity of confining the eigenfunctions used in QuaLiKiz to values of θ between $\pm\pi$.

3.1 Overview of the Gyrokinetic Codes Used

3.1.1 QuaLiKiz

The code QuaLiKiz¹² is a very fast quasilinear gyrokinetic code, capable of calculating the instability characteristics of one wavenumber for a given set of plasma parameters in about 1 s using one CPU,⁹ as also observed during this investigation. QuaLiKiz was and is being compared extensively against nonlinear codes such as GS2¹² or GYRO,¹³ showing agreement in a broad parameter range. An overview is presented in Ref. 11.

To obtain the instability characteristics, QuaLiKiz solves the linear gyrokinetic equation in the electrostatic case, as presented in Sec. 2.2.1, using the formalism of angular and action variables. Hence, the problem is reduced to three dimensions with the particle energy, the pitch angle, and the radial coordinate remaining.²¹ The magnetic geometry of QuaLiKiz corresponds to the s - α -geometry described in Sec. 2.2.3.1. To speed up calculations, the eigenfunctions of the perturbed electrostatic potential are assumed to be strongly ballooned at the low field side, allowing the use of a Gaussian function¹² $\phi = \phi_0 \exp(-\theta^2 w^2 / 2d^2)$ confined to poloidal angles θ between $\pm\pi$. Although this approach was benchmarked against GS2 and GYRO,¹² deviations could occur in the limit of low magnetic shear and high values of the α -parameter.

Solutions to the gyrokinetic equation are found using an eigenvalue solver, which determines the number of eigenvalues and their approximate value inside a closed contour in the complex plane, thus allowing to find all unstable modes.¹² This approach becomes increasingly difficult for modes close to the real axis, i.e. for modes with a low growth rate. Using the unstable modes obtained, the fluxes of energy, particles, and momentum are constructed by summation over all modes using a nonlinear saturation rule tuned to nonlinear simulations. Hence, a small discrepancy in the growth rate obtained for one single mode does not necessarily result in a deviation of the particle fluxes.

3.1.2 GENE

The *Gyrokinetic Electromagnetic Numerical Experiment*^{33–35} (GENE) is a gyrokinetic code, which can be used either in a nonlinear or a linear form, both of which have been shown to yield reliable results.³⁴ The equations solved are presented extensively in Refs. 33–35. As opposed to QuaLiKiz, the particle distribution function is evaluated in five-dimensional phase space, where only gyroaveraging has been taken into account. Thus, velocity space is reduced to two dimensions, with the parallel component and the magnetic moment remaining. However, the calculations can be sped up by process parallelization across five phase space dimensions as well as across the number of particles considered.

The evaluation of the gyrokinetic equation can be performed using an initial value solver or an eigenvalue solver. Whereas the latter resolves an arbitrary number of unstable modes, the initial value solver only finds the most unstable solution, as this is the mode determining the evolution of the system. However, as opposed to the eigenvalue solver, the initial value solver allows real time monitoring of the calculation process and thus identification of instabilities far from reaching convergence. With the eigenvalue solver, such an assessment is not possible until the calculation has converged. This can be problematic close to the instability threshold, where the evaluation of the gyrokinetic equations is generally more difficult. As the use of the initial value solver is consequently more robust, the following investigation will be performed using GENE with the initial value solver.

To calculate the instability characteristics, GENE uses a field aligned coordinate system, with x being the radial coordinate of the flux surface, y the binormal direction labeling the field lines on a flux surface, and z the parallel direction along the field line.^{35,36} Due to differences with respect to the coordinate system (r, θ, φ) of QuaLiKiz, wavenumbers k_θ used in QuaLiKiz have to be converted to GENE wavenumbers k_y to enable comparison of instability characteristics. In the limit of low inverse aspect ratios ϵ and typical values of the safety factor q , the exact conversion $k_y = k_\theta(1 + (\epsilon/q)^2)^{1/2}$ can be approximated by $k_y \approx k_\theta$, with the error being below 1 %.

As the physics included is more complete as compared to QuaLiKiz, evaluation of the underlying equations takes significantly longer, ranging from 10^3 CPUs for strong instabilities up to 10^6 CPUs in extreme cases of very low growth rates. However, the typical slow-down as observed in this investigation is in the order of 10^4 as compared to QuaLiKiz running with identical plasma parameters.

3.2 Determination of the Regime of Discrepancy between both Codes

The discrepancy in growth rates is to be mapped out in the regime of low magnetic shear s and high values of the α -parameter for toroidal ITG modes. For this purpose, combinations of six values of $s \in \{-0.2, 0.1, 0.4, 0.6, 1.0, 1.5\}$ and nine equally spaced values of the α -parameter between 0 and 0.8 are chosen, corresponding to the approximate range reported in Ref. 13. The investigation is carried out for three values of $k_\theta \approx k_y$, being 0.1, 0.3, and 0.5, since the most unstable wavenumbers are found between 0.1 and 0.3.²⁵ Note that the wavenumbers k_y and k_θ are normalized to ρ_i^{-1} . This notation will be used in the following analysis, if not mentioned otherwise.

Since the choice of values for the three parameters requires the analysis of 162 different combi-

Table 3.1: Plasma and machine parameters used for the comparison of QuaLiKiz and GENE around the Cyclone DIII-D base case parameter set.³⁷ The simulations considered two particle species, being deuterium ions and electrons. Note that both the density and the electron temperature gradients were reduced with respect to the original Cyclone base case parameters to suppress the occurrence of trapped electron modes.

n_i/n_e	T_i/T_e	R/L_n	R/L_{T_e}	q	β	B	r/R	v
1	1	1	3	1.4	0	3 T	1/6	0

nations, the investigation is carried out for only one fixed set of plasma and machine parameters, based on the *Cyclone DIII-D base case parameter set*.³⁷ The Cyclone base case represents an ITER-relevant DIII-D scenario at mid radius and has been used as a benchmark scenario for approximately the past 20 years. The exact parameters used in this work are presented in Table 3.1. Both the density and the temperature of deuterium ions and electrons are considered identical. Note that the calculations are performed using dimensionless units. To suppress the occurrence of trapped electron modes, the respective driving density and temperature gradients are chosen to be located well below the instability threshold and thus do not correspond to the Cyclone base case parameters. Since the time scales of turbulent fluctuations are significantly shorter than typical collision times ν^{-1} , the plasma is considered collisionless. Note that this set of parameters is not self-consistent, as the normalized plasma pressure β is set to zero for the GENE calculations to allow for a comparison with QuaLiKiz at similar settings.

Using the parameters presented, the growth rates of instabilities and the corresponding eigenfunctions are calculated for each combination of the magnetic shear, the α -parameter, and the wavenumber k_y or k_θ as a function of the normalized ion temperature gradient R/L_{Ti} . The range of normalized ion temperature gradients considered is chosen such that the instability threshold as well as the behavior far from the threshold is captured. An example of three scans as performed by QuaLiKiz is illustrated in Fig. 3.1.

3.2.1 Comparison of the Instability Growth Rates

An instability is characterized by both its threshold gradient, as well as by the sensitivity of the growth rate to the driving gradient above the threshold. However, the derivation of the instability threshold gradient from only results close to the threshold is susceptible to numerical uncertainties, as the calculation of weakly growing instabilities becomes increasingly difficult. Additionally, in the case of QuaLiKiz solutions may not be found close to the threshold, as e.g. for the parameter choice $k_\theta = 0.1$, $s = 1.5$, $\alpha = 0$, illustrated in Fig. 3.1 (red points). Hence, extrapolation from numerically stable results down to the threshold is required to determine the threshold reliably. Since in the limit of strongly driven instabilities, the growth rate increases as $(R/L_{Ti})^{1/2}$, cf. Eq. (2.55), a corresponding function is used for extrapolation. This approach usually represents the data obtained from calculations well, as e.g. for the parameter choice of $k_\theta = 0.1$, $s = 0.4$, $\alpha = 0.2$ calculated with QuaLiKiz, cf. Fig. 3.1 (blue points). However, if only a limited number of reliable results close to the threshold is available for analysis, a second order polynomial is used instead to determine the value of the normalized ion temperature gradient at the threshold of the instability through extrapolation. In this case the convergence of the data fitting procedure is better for a second order polynomial as opposed to a square root function. An example where extrapolation utilizing a second order polynomial is suitable is illustrated in Fig. 3.1 for QuaLiKiz calculations using the parameters $k_\theta = 0.1$, $s = 0.1$, $\alpha = 0$ (green points).

Alternatively, instabilities can be described by the value of the instability growth rate at a fixed value of the ion temperature gradient far from the instability threshold. This method is more robust than characterization using the value of the ion temperature gradient at the instability threshold, since the results used are considered numerically stable. However, since the choice of R/L_{Ti} is arbitrary for this method, conclusions regarding the agreement between QuaLiKiz and GENE can only be drawn by analyzing the change of the growth rate for different values for the magnetic shear or the α -parameter, or by combining this characterization method with the characterization utilizing the value of the ion temperature gradient at the instability threshold. A direct comparison of the absolute values of the growth rates for a fixed value of R/L_{Ti} between QuaLiKiz and GENE has to be made with care, as possible agreement may be attributed to the choice of R/L_{Ti} . An example of this effect is given by the growth rates obtained with QuaLiKiz for the parameter combinations $k_\theta = 0.1$, $s = 0.4$, $\alpha = 0.2$ and $k_\theta = 0.1$, $s = 1.5$, $\alpha = 0$ for $R/L_{Ti} = 13$, cf. Fig. 3.1 (blue and red points). Although both growth rates in this example agree within 1 %, suggesting identical behavior of the instability, the instability characteristics differ strongly, rendering a direct

comparison vain. Therefore, comparing the absolute values of the growth rates calculated by QuaLiKiz and GENE requires an integrated assessment using the analysis of the instability thresholds or of the change of growth rates for different values of the magnetic shear and the α -parameter.

In this investigation, a value of $R/L_{T_i} = 10.0$ is used to compare the growth rates of different parameters at a fixed value of the ion temperature gradient, since this value is high enough to ensure numerical stability of the growth rates obtained, while being sufficiently close to the instability threshold to not be dominated completely by the analytic solution of the strongly driven linear gyrokinetic equation. Regarding the analysis of QuaLiKiz calculations, the value of the growth rate at $R/L_{T_i} = 10.0$ is obtained through fitting, since individual data points may be shifted up or downwards with respect to the function describing the data points or as solutions may not have been found. Both cases are illustrated in Fig. 3.1. Although the use of a fitting function would have only been necessary in 19 of the 162 QuaLiKiz calculations, all QuaLiKiz scans were analyzed in this manner. In the cases where fitting would not have been necessary, deviations to the actual values calculated by QuaLiKiz were found to be negligible, as the fitting functions described the data very well. Therefore, this approach was chosen as it allowed for an easier analysis since no differentiation had to be made between both case and a suitable fitting function was already found during the determination of the instability threshold gradient. As for the results obtained with GENE, the values of the growth rate at $R/L_{T_i} = 10.0$ are considered accurate, since the results were found to not exhibit numerical errors.

Finally, characterization of the instability using the stiffness $d\gamma/d(R/L_{T_i})$ of the growth rate at the instability threshold was dismissed, as this method is strongly dependent on the function used for extrapolation and requires an increased number of data points, which may not be available in the case of GENE. Consequently this approach is not reliable to compare instabilities for different values of the parameters considered.

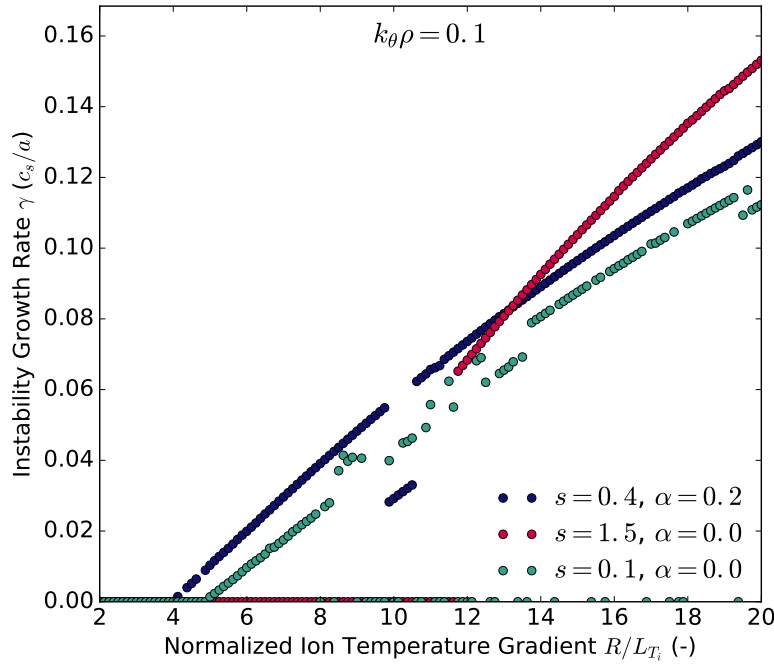


Fig. 3.1: R/L_{T_i} -scans with QuaLiKiz for three different combinations of the magnetic shear s and the α -parameter for the plasma parameters listed in Table 3.1. Usually, the data points of scans can be represented by a function of the form of a square root down to the instability threshold (blue points). However, sometimes solutions close to the threshold are not found for entire segments (red points) or for individual data points (green points). It may also occur, that entire segments (blue points) or individual data points (green points) are shifted up- or downwards with respect to the expected behavior. Therefore, both the instability threshold and the growth rate at a certain value of the ion temperature gradient can only be obtained by extrapolation from the robust regions of the growth rate calculation.

3.2.2 Comparison of the Eigenfunctions

Since the perturbed particle distributions functions δf were found to be linearly dependent on the perturbed electrostatic potential $\delta\phi$ in the gyrokinetic equation, the eigenfunctions calculated by both codes should agree to ensure identical responses of the particle distribution function. Disagreement between both solutions of the perturbed electrostatic potential could thus be responsible for differences in the growth rates and fluxes observed.

Whereas the eigenfunctions used in QuaLiKiz are approximated by a Gaussian function characterized by two parameters, being the mode width w and the distance d between resonant surfaces, GENE obtains a non-analytic solution for the perturbed electrostatic potential. However, since the modes considered are strongly ballooned at the low field side, the solutions for the electrostatic potential typically behave similarly and can thus be approximated by a single Gaussian as well. Therefore, the $1/e$ -half width of the Gaussians can be used to compare both eigenfunctions. Since the approach used in QuaLiKiz is confined to values of the poloidal angle θ between $\pm\pi$, the non-analytic solution obtained by GENE is fitted to a single Gaussian function using only the values between these boundaries, enabling comparison in the regime relevant to QuaLiKiz. A second fitting function covers the entire θ -range considered by GENE, thus being sensible to eigenfunctions peaked at values other than $\theta = 0$, as e.g. in the case of slab-type modes.

3.3 Validation of Accuracy

Numerical Accuracy The calculations performed with QuaLiKiz and GENE are desired to be both fast and accurate. Yet, a speed-up of the calculations is obtained by decreasing the accuracy of the calculations. In the case of the fast code QuaLiKiz, time limitations are not an issue, wherefore a relatively high number of at maximum 5×10^6 integrand evaluations of the two dimensional integrals as well as a high relative accuracy of the one and two dimensional integrals, being 1×10^{-4} and 2×10^{-3} respectively, are set for all calculations performed.

For the slow code GENE however, decreasing the computation time necessary is vital to perform the large amount of calculations needed for this investigation. Hence, the minimum accuracy where results are stable within a few % with respect to an increase in accuracy has to be utilized, requiring intensive benchmarking of the influence of the respective parameters on the stability of the results. The resolution of the fixed five dimensional grid applied is determined by four quantities, being the number of grid points in the radial direction n_{x0} , in the parallel direction n_{z0} , in the direction of the parallel velocity n_{v0} , and in the direction of the magnetic moment n_{w0} . Furthermore, the simulation box can be extended in both the direction of the parallel velocity and the magnetic moment by setting the parameters lv and lw to ensure normalization of the respective Maxwellian integrals. Finally, the numerical dissipation in the parallel direction hyp_z and in the direction of the parallel velocity hyp_v can also be specified. As a result, the influence of eight parameters on the stability of the results has to be reviewed.

Ideally, convergence tests of this kind should be carried out for every calculation performed to ensure reliability of the results obtained. However, in practice this approach is not feasible as the time required may exceed the speed-up gained. Therefore, only two stability analyses were

Table 3.2: Numerical parameters for GENE calculations using s - α -geometry. For each value of the magnetic shear, identical parameters were used for all combinations of the α -parameter and the wavenumber k_y . Note that the resolution in the radial direction n_{x0} includes $k_x = 0$ and an even number of positive and negative k_x -modes.

Magnetic Shear	n_{x0}	n_{z0}	n_{v0}	n_{w0}	lv	lw	hyp_z	hyp_v
-0.2, 0.1, 0.4, 0.6	17	32	128	16	4.0	9.0	0.8	0.2
1.0, 1.5		16	64		3.0			

performed at values of the magnetic shear of -0.2 and 1.0 , with the α -parameter set to 0.8 and the wavenumber k_y set to 0.5 in both cases, since the computational effort increases with decreasing values of the magnetic shear and increasing values of the α -parameter. As convergence is generally easier to achieve for larger growth rates as opposed to instabilities located near the threshold, the stability of the former growth rates was taken as criterion of having achieved convergence in the analyses performed. The numerical parameters used throughout this investigation are listed in Table 3.2 for individual values of the magnetic shear. As the behavior of the plasma was analyzed for decreasing values of the magnetic shear, the resolution in both the parallel direction and the parallel velocity direction was doubled, while the simulation box was extended further in the direction of the parallel velocity. Although all results obtained are consequently subjected to uncertainties, individual errors of the growth rates cannot be specified reliably due to changing parameters used or increasing computational effort closer to the instability threshold. Yet, as a consequence of the convergence analysis, the overall uncertainty should be in the order of at maximum a few %.

Accuracy of the Magnetic Geometry The assessment of the accuracy of the results obtained with GENE is further complicated by the availability of different magnetic geometries implemented. Since QuaLiKiz uses a geometry of shifted, circular flux surfaces, GENE scans were carried out using the geometry `s_alpha`. A comparison with the similar geometry `s_alpha_B` revealed deviations in the order of a few % only, wherefore the standard implementation of the s - α -geometry was utilized for this investigation. However, since the s - α -geometry is not uniformly defined, differences between the implementations used in QuaLiKiz and GENE may exist. Furthermore, the shifted circle equilibrium is generally not self-consistent.³⁵ Therefore, an additional two α -scans per wavenumber for the lowest two choices of the magnetic shear, being -0.2 and 0.1 , were carried out using Miller-geometry³⁸ in GENE. This equilibrium model is completely described by nine parameters, two of which are insignificant for this investigation, namely the elongation and the triangularity. As the s - α -geometry is self-consistent only at low values of the normalized plasma pressure and large aspect ratios R/a ,³⁸ only minor differences between the growth rates obtained with both geometries are expected. The calculation with Miller-geometry utilized the same numerical parameters as in the analysis using the shifted circle model, cf. Table 3.2, with the number of grid points in the direction of the parallel velocity reduced from 128

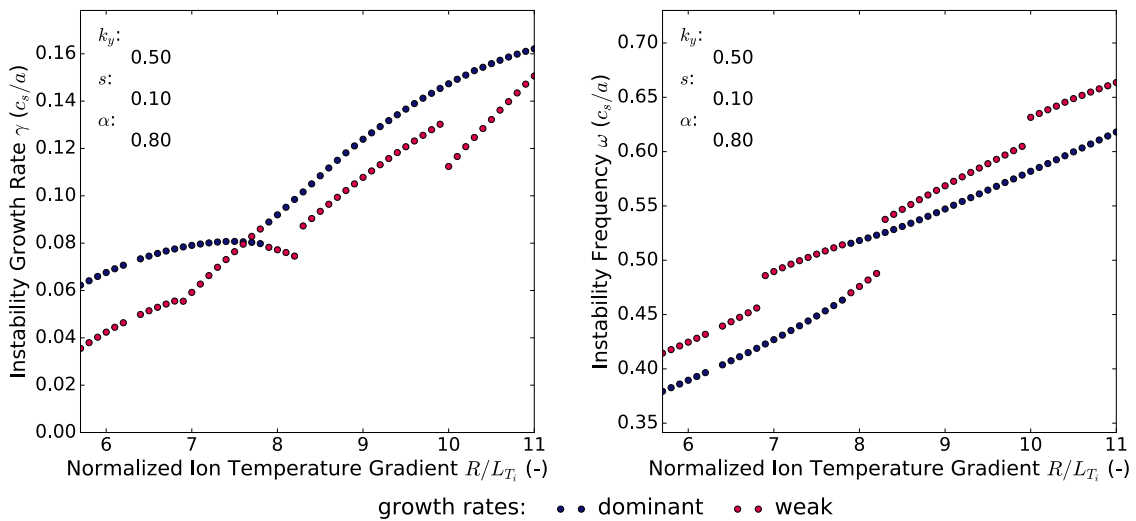


Fig. 3.2: An eigenvalue analysis with GENE for $k_y = 0.5$, $s = 0.1$, $\alpha = 0.8$, determining the two most unstable instabilities in the system for a given value of the normalized ion temperature gradient reveals the presence of multiple modes with clearly separated frequencies. More importantly, the most unstable growth rate (blue points) does generally not correspond to a single mode throughout the R/L_{T_i} -range considered, as the discontinuity in the respective instability frequency shows.

to 64. For further investigation of the effect of different geometries on the stability of the growth rates, the respective calculations are supported by results obtained with the code GKW using Miller-geometry.

Accuracy of Modes Obtained The analysis of the growth rates obtained regarding the threshold value R/L_{Ti} of the instability is hindered by the appearance of multiple modes throughout an R/L_{Ti} -scan. Since the initial value solver captures only the most dominant instability, the mode considered might change throughout the R/L_{Ti} -scan for a given set of parameters, as illustrated in Fig. 3.2. Although the dominant growth rate is continuous throughout the scan, a discontinuity in the instability frequency associated with the dominant growth rate is occasionally observed, identifying the dominant growth rate as consisting of two separate modes, each of which is dominant only in a limited range of R/L_{Ti} values. Considering the second most unstable instability as well, both modes of the dominant growth rate are found to continue as weaker modes upon being surpassed by the other mode. The eigenfunctions of the additional modes captured are not necessarily peaked around ballooning angles of $\theta = 0$ and may exhibit strong contributions at ballooning angles being multiples of 2π , wherefore they may not be found by QuaLiKiz.

Moreover for a given value of the wave number k_y and the magnetic shear s , the curve representing the dominant growth rates, cf. e.g. Fig. 3.2, is approximately shifted up- or downwards with changing values of the α -parameter. In the presence of multiple modes and consequently discontinuities in the first derivative of the curve representing the dominant growth rate, a discontinuity may also be observed when illustrating the threshold values R/L_{Ti} of the instability as a function of the α -parameter for fixed values of k_y and s . This discontinuity is characterized by the appearance of a weakly growing mode well below the threshold value R/L_{Ti} of the curve with $\Delta\alpha = \pm 0.1$. Although low growth rate solutions are not necessarily numerically stable, the modes observed were found not to be numerical phenomena and were thus included in the analysis. A similar behavior has occasionally been observed for solutions obtained with QuaLiKiz as well.

3.4 Analysis of the JET Hybrid Scenario 75225

Whereas the plasma and machine parameters used to determine the regime of discrepancy between QuaLiKiz and GENE are tailored for this investigation, the analysis of a JET scenario with low magnetic shear and a high value of the α -parameter allows for a sensitivity analysis of the results obtained with QuaLiKiz with respect to GENE for practical parameters. For this purpose, the JET hybrid scenario 75225^{39,40} is analyzed at two points of the poloidal cross section, being $r/a = 0.42$ and $r/a = 0.73$, by comparing the instability growth rates obtained with QuaLiKiz and GENE using s - α -geometry as a function of the normalized ion temperature gradient. To support the analysis, both the results of the preceding growth rate investigation, as well as the eigenfunctions obtained for the JET parameters are used for further assessment.

Since hybrid scenarios are characterized by a flat q -profile in the plasma center, the point located in the inner half radius has a significantly lower value of the magnetic shear than the point located further out, cf. Table 3.3. Consequently, agreement in the growth rates obtained with QuaLiKiz and GENE is only expected to occur for the outer location. However, during previous analyses,^{14,39} agreement was also observed at the inner location by neglecting the effect of α -stabilization by QuaLiKiz, setting $\alpha = 0$. Therefore, the investigation of the JET hybrid scenario is carried out examining both the original parameters as well as the case of a vanishing α -parameter in separate calculations. A full list of the parameters used for this analysis is presented in Table 3.3. As opposed to the investigation of the regime of discrepancy between QuaLiKiz and GENE, collisions are taken into account in the analysis of the JET hybrid scenario.

Table 3.3: Parameters of the JET hybrid scenario analyzed at two radial positions, located inside and outside of the half radius. Here, the geometric major radius is denoted by R_{geo} . The value of the major radius denoted by R is dependent on the radial position due to the Shafranov shift. The quantity ρ describes the normalized toroidal flux coordinate. The plasma considered contains a small fraction of ^{12}C . Note that the actual values for both the density n and the normalized ion density gradient R/L_{n_i} used for the calculations were specified with a significantly higher accuracy to ensure quasi-neutrality of the plasma.

Inner Location $r/a = 0.42$				Outer Location $r/a = 0.73$		
Common Parameters:						
B (T)				1.85		
R_{geo} (m)				3.11		
a (m)				0.96		
Location Dependent Parameters:						
R (m)		3.07		2.99		
ρ		0.38		0.68		
q		1.39		2.12		
s		0.39		1.28		
α		0.70		0.62		
Particle Species Dependent Parameters:						
	Electrons	Deuterium	Carbon	Electrons	Deuterium	Carbon
n (10^{19} m^{-3})	4.30	3.48	0.14	3.45	2.98	0.08
T (keV)	4.40	4.70	4.70	2.40	2.64	2.64
R/L_n	1.91	2.08	1.18	3.24	2.05	10.82
R/L_T	5.80	4.33	4.33	7.10	8.54	8.54

4 Comparison of Growth Rate Calculations with QuaLiKiz and GENE

In this section, the results of the instability calculations using QuaLiKiz and GENE, as described in the previous section, are presented. The regime of disagreement between the solutions obtained with both codes is identified by analyzing the instability threshold gradients in Sec. 4.1.1 as well as the instability growth rate at a constant value of the normalized ion temperature gradient in Sec. 4.1.2. In the $s - \alpha$ -range considered, the widths of the eigenfunctions are compared in Sec. 4.2 regarding explaining the observed behavior of the growth rates. Using these analyses, sources for the discrepancy of growth rates between both codes are discussed in Sec. 4.3. Furthermore, in Sec. 4.4 the behavior of QuaLiKiz for practical parameters used in the JET hybrid scenario 75225 is compared to the findings of the investigation regarding the disagreement of both codes.

4.1 Growth Rate Comparison

4.1.1 Threshold Values of the Instability

The instability threshold of the normalized ion temperature gradient has been determined in the regime of s between -0.2 and 1.5, with the α -parameter ranging from 0 to 0.8. For all three values of the wavenumber k_y considered, the results are summarized in Fig. 4.1.

In agreement with expectations, destabilization by an increase of the α -parameter for a constant magnetic shear occurs for larger values of $s - \alpha$, whereas an increase of α in the regime of lower values of $s - \alpha$ results in a stabilization of the instability, necessitating a larger value of the normalized ion temperature gradient for an instability to develop. This behavior is observed for both the results obtained with QuaLiKiz and with GENE. Furthermore, stabilization by a decrease of the magnetic shear s for a fixed value of the α -parameter occurs for low values of $s - \alpha$, whereas for larger values of $s - \alpha$, an increase in s stabilizes the system.

The instability threshold gradients obtained with both codes are generally in good agreement above $s - \alpha \approx 0.2$ with the instability threshold calculated by QuaLiKiz agreeing within 20% with GENE calculations. Whereas this behavior is observed for all values of s and α above this limit in the case of $k_y = 0.1$, for larger values of the wavenumber, the destabilizing impact of the α -parameter is overestimated by QuaLiKiz for $s = 1.0$ and $s = 1.5$. In these cases, the instability threshold obtained decreases only weakly with increasing values of the α -parameter as compared to the rate of change at very low values of $s - \alpha$. However, for negligible values of the α -parameter, the solutions with QuaLiKiz and GENE obtained are still in good agreement for $s = 1.0$ and $s = 1.5$.

Severe disagreement between the results obtained with QuaLiKiz and GENE is observed for $s - \alpha \lesssim -0.2$. In this regime, deviations are typically greater for lower wavenumbers, especially for $k_y = 0.1$ where instability thresholds as calculated by QuaLiKiz are off by more than 100%. For increasing values of k_y , the maximum deviations found are brought down to about 90% for $k_y = 0.3$ and 60% for $k_y = 0.5$ as compared to the instability thresholds calculated with GENE using shifted-circle geometry. Analyzing the dependence on the magnetic shear, disagreement for identical values of $s - \alpha$ but different combinations of s and α is often worse for lower values of the magnetic shear as compared to larger values for identical wavenumbers, as in the case of $k_y = 0.1$. However, the behavior described is observed far less frequent for $k_y = 0.3$ or $k_y = 0.5$. Moreover, instability threshold gradients calculated with QuaLiKiz for constant values of the wavenumber are more consistent for $k_y = 0.3$ and $k_y = 0.5$, where deviations between instability threshold gradients for

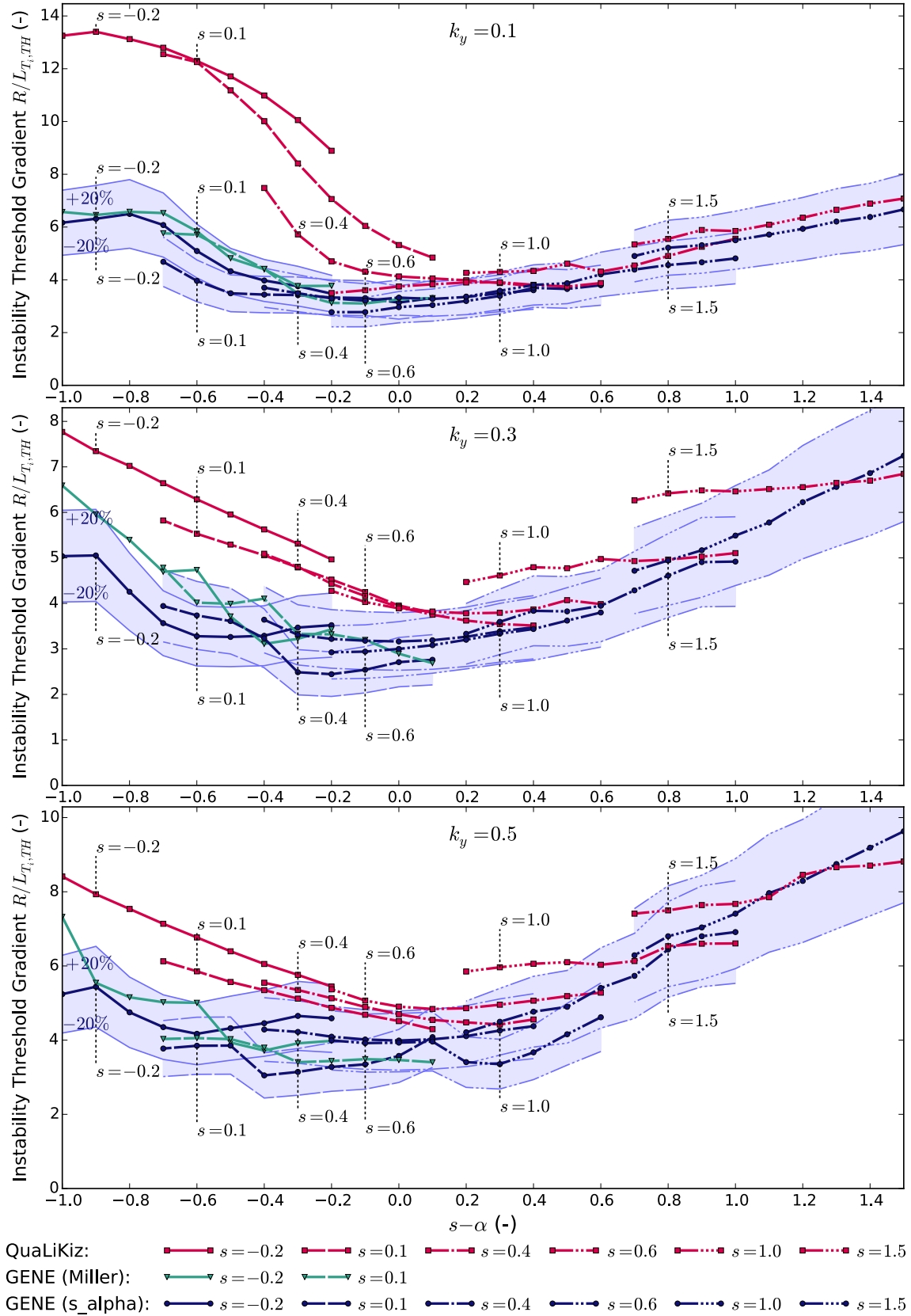


Fig. 4.1: Dependence of the instability threshold gradient R/L_{T_i} on $s - \alpha$, calculated for three different wavenumbers using QuaLiKiz (red), GENE with $s - \alpha$ -geometry (blue), GENE with Miller-geometry (green), and GKW with Miller-geometry (orange).

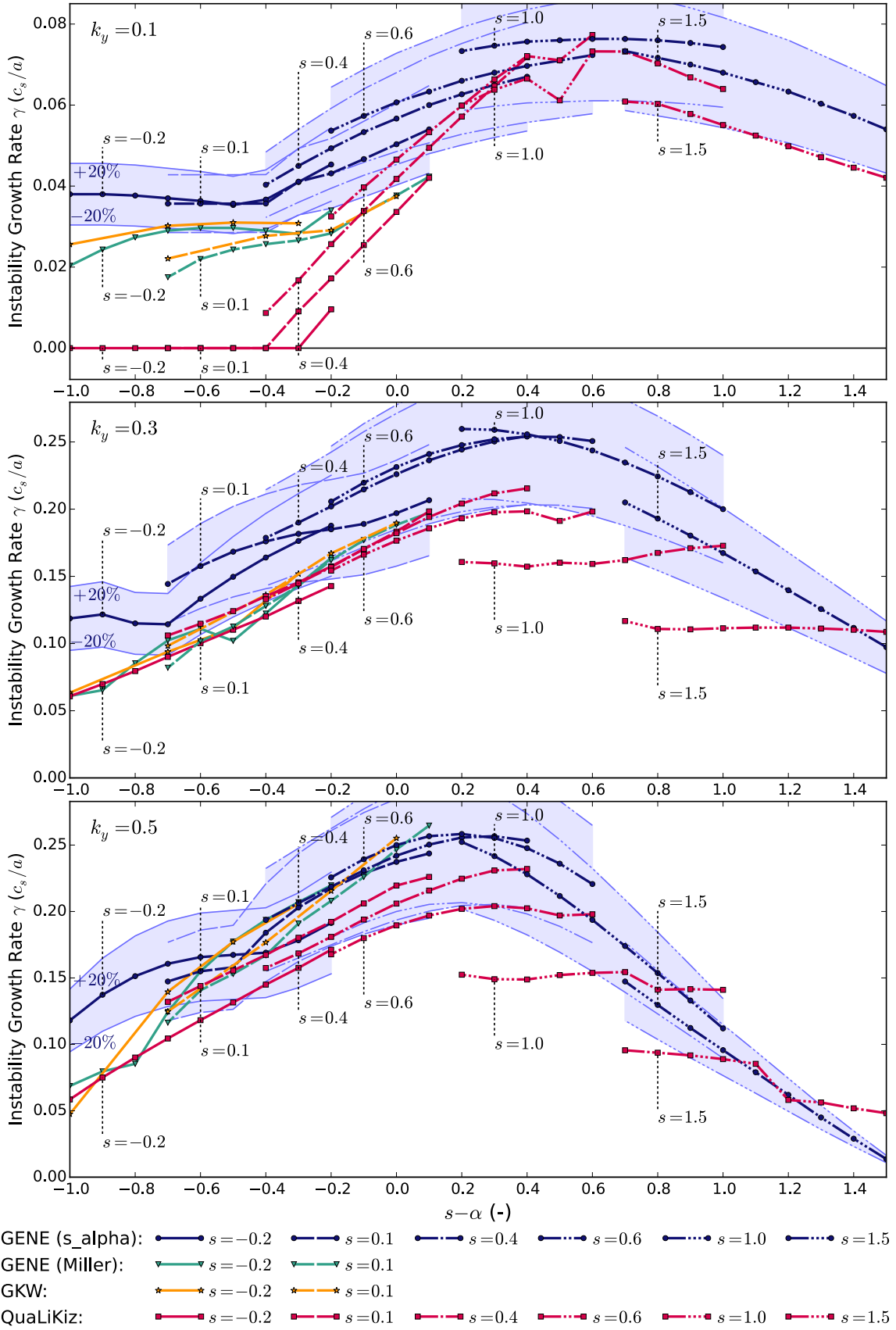


Fig. 4.2: Dependence of the instability growth rate on $s - \alpha$ for a fixed value of the normalized ion temperature gradient of $R/L_{Ti} = 10.0$, calculated for three different wavenumbers using QuaLiKiz (red), GENE with $s - \alpha$ -geometry (blue), GENE with Miller-geometry (green), and GWK with Miller-geometry (orange).

identical values of $s - \alpha$ are less severe as opposed to the case of low wavenumbers. Consequently, the disagreement between QuaLiKiz and GENE using s - α -geometry and the consistency of results obtained with QuaLiKiz for different combinations of s and α is worse for low wavenumbers $k_y = 0.1$ as opposed to larger wavenumbers.

The effect of the different geometries used for GENE calculations, i.e. the shifted-circle equilibrium and Miller-geometry, on the instability threshold gradients obtained is minor. Nevertheless, applying Miller-geometry yields almost consistently noticeably larger threshold gradients as opposed to s - α -geometry, resulting in slightly better agreement with the results obtained by QuaLiKiz, especially for very negative values of $s - \alpha$. This behavior is in so far unexpected, as the differences between both geometries themselves are considered small, due to the case of a large aspect ratio and a negligible normalized pressure gradient β . However, inconsistencies between the s - α -model and an MHD equilibrium in the order of the inverse aspect ratio have been reported before, cf. e.g. Ref. 41.

The comparison of the instability threshold gradients between QuaLiKiz and GENE, as well as between both GENE geometries is complicated by the appearance of dents in the curves obtained with GENE for low values of the magnetic shear for both geometries. Whereas the overall decrease of the instability threshold gradient as a function of $s - \alpha$ can be described roughly by a parabola, in the case of $k_y = 0.3$ the α -scans for $s = -0.2$ and $s = 0.1$ exhibit excursions to lower values of the threshold gradient as expected by extrapolation. This effect is even more prominent for $k_y = 0.5$, where α -scans with values of the magnetic shear of -0.2 , 0.1 , and 0.4 are affected. Throughout the R/L_{Ti} -scans performed with GENE for constant values of s and α , additional low growth rate modes appeared well below the threshold gradient observed for neighboring values of the α -parameter. Consequently, the instability threshold is suddenly shifted downwards upon appearance of such a mode, resulting in excursions to lower values, as described in Sec. 3.3. However, as the nature of these modes is not evident, the analysis of the α -scans demonstrating this behavior is subjected to additional uncertainties.

4.1.2 Growth Rates at a Fixed Ion Temperature Gradient

From the R/L_{Ti} -scans performed, the instability growth rates calculated for a normalized ion temperature gradient $R/L_{Ti} = 10$ are additionally analyzed to assess the agreement of QuaLiKiz with more complete modeling using GENE with both shifted-circle geometry and Miller-geometry, as well as using GKW with Miller-geometry. The respective instability growth rates are summarized in Fig. 4.2 for all three values of the wavenumber.

Analyzing the growth rates at $R/L_{Ti} = 10$, the expected behavior of α -destabilization at larger values of $s - \alpha$ and α -stabilization at lower values of $s - \alpha$ is found for all gyrokinetic codes used, being in agreement with the analysis of the instability threshold gradients of the previous part. The same holds for the influence of the magnetic shear on the stability of the system.

The agreement of the growth rates obtained by QuaLiKiz and GENE with s - α -geometry is within $\sim 20\%$ down to values of $s - \alpha \approx 0.0$. However, the effect of s - α -stabilization is almost consistently overestimated by QuaLiKiz, resulting in lower growth rates as compared to GENE. As in the analysis of the instability threshold gradients, the destabilizing influence of finite values of the α -parameter is not observed for values of the magnetic shear of $s = 1.0$ and $s = 1.5$ for both $k_y = 0.3$ and $k_y = 0.5$. Instead, the growth rates remain virtually constant throughout the α -scan. For negative values of $s - \alpha$, the disagreement between QuaLiKiz and more complete modeling is severe only at very negative values of $s - \alpha \lesssim -0.8$ for $k_y = 0.3$ and $k_y = 0.5$, where the effect of s - α -stabilization is even more overestimated. In between this limit and the boundary of agreement mentioned previously, the agreement is still good, being within $\sim 20\%$. This is especially the case when comparing the growth rates of QuaLiKiz with those obtained using Miller-geometry. For $k_y = 0.3$, the agreement is almost exact, while for $k_y = 0.5$, the agreement is still better as opposed to a comparison with GENE using s - α -geometry. This holds for the growth rates obtained with both implementations of Miller-geometry in GENE and GKW. Slight deviations between GENE

and GKW are due to small differences of 1.7% in the wavenumbers used, due to the conversion from the GENE to the GKW coordinate system. However, as the instability threshold gradients obtained for QuaLiKiz and GENE with Miller-geometry do not exhibit the degree of agreement as observed in the comparison of the growth rates at $R/L_{Ti} = 10$, the good agreement in the latter case has to be attributed at least partially to the choice of R/L_{Ti} . Nevertheless, even for varying values of the ion temperature gradient the growth rates obtained with QuaLiKiz agree better with those obtained using Miller-geometry rather than with those obtained using GENE s - α -geometry.

In the case of low wavenumbers of $k_y = 0.1$ and negative values of $s - \alpha$, the behavior predicted by all codes is fundamentally different. Using GENE with shifted-circle geometry, the growth rates obtained remain independent of the magnetic shear s and the choice of α at a constant level for $s - \alpha \leq -0.4$, whereas QuaLiKiz predicts a stable situation. The codes using Miller-geometry produce results in between those two extrema, yielding decreasing growth rates with increasing values of the α -parameters, although at a significantly lower rate as in the case of larger values of $s - \alpha$. Note that a constant growth rate, independent of the value of the α -parameter is also obtained by GENE using s - α -geometry for larger wavenumbers of $k_y = 0.3$ in the case of a negative magnetic shear for $s - \alpha \leq -0.7$. However, as for $k_y = 0.1$, the disagreement with the other codes used in the regime of negative values of $s - \alpha$ is worse as opposed to larger wavenumbers, as also observed in the analysis of the instability threshold gradients.

4.2 Eigenfunction Comparison

For further interpretation of the analysis of the instability growth rate at a constant value of the ion temperature gradient of $R/L_{Ti} = 10.0$, the solutions of the electrostatic fluctuations obtained are analyzed. Although the eigenfunctions calculated by GENE are non-analytic, they can roughly be approximated by a Gaussian function, allowing for a simple comparison with the Gaussian eigenfunctions used in QuaLiKiz. Since the ansatz used in QuaLiKiz restricts the eigenfunctions to ballooning angles θ between $\pm\pi$, the solutions of the electrostatic fluctuations obtained with GENE are fitted to two different Gaussian functions, one considering the entire θ -range covered, whereas the second function only takes solutions in the same regime as QuaLiKiz into account. Using the $1/e$ -half width of the Gaussian functions obtained, the eigenfunctions of both codes can be easily compared, as presented in Fig. 4.3.

Analyzing the width of the eigenfunctions obtained, the solutions found with both QuaLiKiz and GENE increase in width with increasing values of $s - \alpha$ until a certain value of $s - \alpha$ is reached, above which the width of the eigenfunctions decreases. Furthermore, the solutions obtained with QuaLiKiz are typically more narrow as opposed to GENE eigenfunctions. In these two ways, the behavior of the eigenfunction width resembles the trend of the instability growth rate at the same constant value of R/L_{Ti} , cf. Fig. 4.2. In the case of QuaLiKiz, the maximum width of the eigenfunctions is located around $s - \alpha \approx 0.4$, agreeing very well with the location of the maximum instability growth rates found. Nevertheless, the magnitude of the eigenfunction width is not directly linked to the growth rate, since the broadest eigenfunctions are found for $k_y = 0.1$, which is characterized by the lowest growth rates obtained. More importantly, the growth rates for $k_y = 0.3$ and $k_y = 0.5$ are of similar magnitude with neither wavenumber constantly having larger growth rates throughout the $s - \alpha$ -range considered as compared to the other wavenumber, whereas the eigenfunctions obtained for $k_y = 0.3$ are constantly broader as opposed to the eigenfunctions obtained for $k_y = 0.5$. However, a similar correlation of the maximum eigenfunction width and the maximum growth rate is not found in the case of GENE, wherefore no obvious correlations between these two quantities are assumed for both GENE and QuaLiKiz. Nevertheless, the behavior of the roughly constant growth rates found for $s = 1.0$ and $s = 1.5$ in the case of $k_y = 0.3$ and $k_y = 0.5$ is also observed for the width of the respective eigenfunctions.

Comparing the width of both Gaussian functions used to represent the solutions found with GENE, the eigenfunctions calculated by GENE are confined to ballooning angles θ between $\pm\pi$

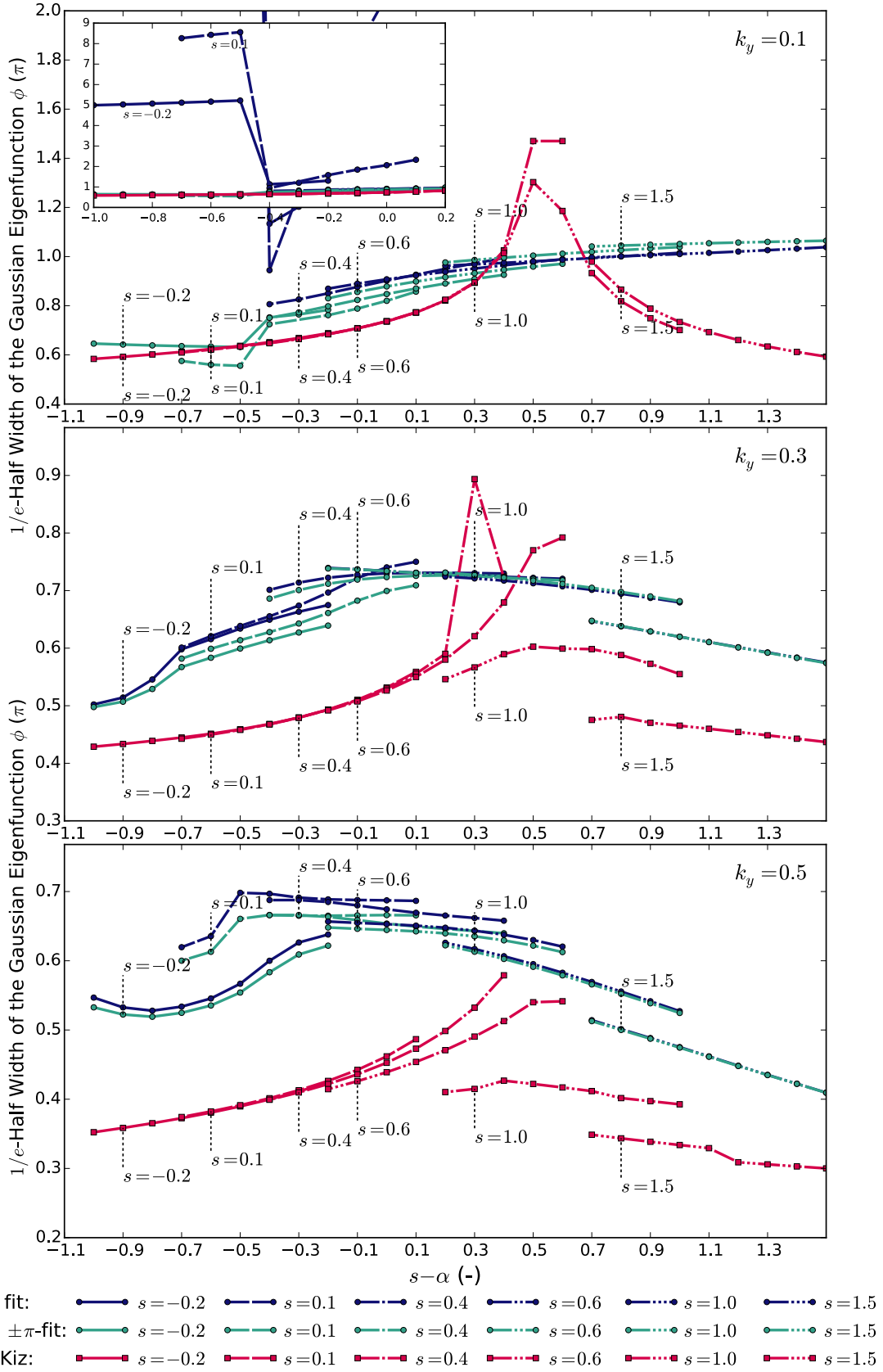


Fig. 4.3: Dependence of the $1/e$ -Half Width of the Gaussian Eigenfunctions on $s - \alpha$ for a fixed value of the normalized ion temperature gradient of $R/L_T = 10.0$, calculated for three different wavenumbers using QuaLiKiz (red), GENE with s - α -geometry (blue), and GENE with Miller-geometry (green).

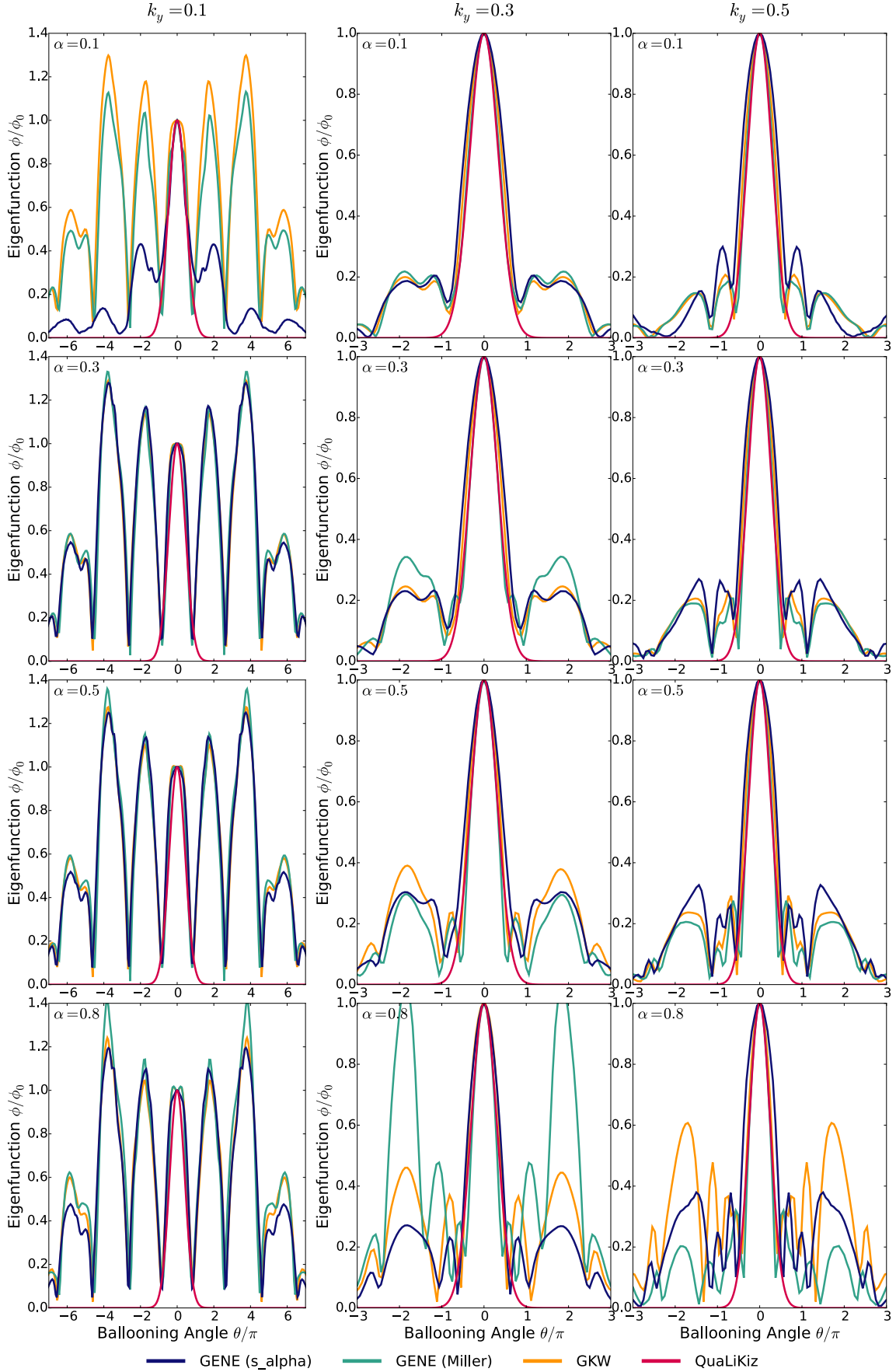


Fig. 4.4: Normalized eigenfunctions for negative values of the magnetic shear $s = -0.2$, four values of the α -parameter, and a normalized ion temperature gradient of $R/L_{T_i} = 10.0$, calculated for three different values of the wavenumber using QuaLiKiz (red), GENE with s - α -geometry (blue), GENE with Miller-geometry (green), and GWK with Miller-geometry (orange).

in the case of large values of the magnetic shear and for large wavenumbers, where both Gaussian functions used are of identical width, cf. e.g. $s = 1.5$ for $k_y = 0.3$ or $k_y = 0.5$ in Fig. 4.3. Modes with smaller values of s have small, but finite contributions at $\theta = \pm 2\pi$, shifting the width of the Gaussian eigenfunctions to larger values. This effect is especially prominent in the case of $k_y = 0.5$ for negative values of s , where the influence of contributions located at $\theta \neq 0$ grows with increasing values α (cf. shape of the eigenfunctions for different values of the α -parameter in Fig. 4.4). In the case of $k_y = 0.1$, the assumption of having strongly ballooned eigenfunctions breaks down for $s - \alpha \lesssim -0.5$. Instead, the modes observed are located around ballooning angles being multiples of $\pm 2\pi$ with contributions from $\theta = \pm 4\pi$ dominating, as illustrated in Fig. 4.4. Consequently, these instabilities are slab-type ITG modes as opposed to the curvature-type ITG modes captured for the other parameters investigated. The validity of the slab-type ITG modes observed was confirmed by GENE using Miller geometry and by GKW, cf. Fig. 4.4, both of which are reported of obtaining broad eigenfunctions in the parameter range of low magnetic shear and low wavenumbers, cf. Ref. 13. Analyzing the behavior of the instability growth rates for both GENE using shifted-circle geometry and QuaLiKiz in the $s - \alpha$ -range where the slab-type ITG modes occur, the respective GENE growth rates exhibit the plateau behavior at a finite value as addressed in the previous part, whereas QuaLiKiz predicts a stable situation, cf. Fig. 4.2. Therefore, the difference in growth rates observed is due to the presence of slab-type ITG modes, which QuaLiKiz cannot resolve.

Although the instability growth rates obtained with QuaLiKiz are best represented by GENE calculations using s - α -geometry, the differences in eigenfunctions obtained between the three codes QuaLiKiz is validated against are only minor in the case of negative values of the magnetic shear, cf. Fig. 4.4. Nevertheless, it should be noted that in the regime relevant to QuaLiKiz, i.e. for ballooning angles between $\pm \pi$, using GENE with Miller geometry yields the narrowest eigenfunctions, whereas the solutions found for GENE with shifted-circle geometry are broadest. However, the differences of the eigenfunctions observed are not sufficient to explain deviations in growth rates between the GENE and GKW.

4.3 Discussion

In the previous two sections, the instability threshold gradients, the growth rates at a constant value of the ion temperature gradient, and the eigenfunctions as calculated by QuaLiKiz and both GENE and GKW have been analyzed. The differences found and their consequences for QuaLiKiz will be discussed in this section.

Consistent Overestimation of s - α -Stabilization Although the instability threshold gradients and growth rates obtained with QuaLiKiz agree within 20% with the respective results found with GENE using s - α -geometry for positive values of $s - \alpha$, the effect of s - α -stabilization is consistently overestimated for QuaLiKiz throughout the entire $s - \alpha$ -range considered, yielding larger threshold gradients and lower growth rates. Moreover, the width of the Gaussian electrostatic fluctuations used by QuaLiKiz is also almost consistently underestimated as compared to GENE using shifted-circle geometry, GENE using Miller-geometry, or GKW. Consequently, modifying the ansatz used in QuaLiKiz to consider broader eigenfunctions may yield a better agreement.

Increased Disagreement for Negative Values of $s - \alpha$ Both the instability threshold gradients and to a lower extend the growth rates at a constant value of R/L_{T_i} calculated with QuaLiKiz show increased disagreement for negative values of $s - \alpha$ as compared to GENE using shifted-circle geometry, GENE using Miller-geometry, and GKW. However, as the deviations of QuaLiKiz with respect to codes utilizing Miller-geometry are less severe as opposed to GENE using s - α -geometry, differences in the calculation of the drift-frequency due to different implementations of the geometry used may be responsible for the discrepancy observed, since this term becomes relevant at low values of $s - \alpha$. Consequently, a further investigation of the exact implementations

of both geometries is necessary to assess if differences in the drift-frequency are responsible for the deviations.

Weak α -Destabilization for Both Large s and Wavenumbers The growth rates calculated with QuaLiKiz in the case of magnetic shears of $s = 1.0$ and $s = 1.5$ for $k_y \geq 0.3$ were found to depend only weakly on the α -parameter, resulting in a virtually constant growth rate throughout the respective α -scans performed. This behavior may be due to an improper pitch angle integration of transit and drift frequencies in the case of passing particles. In QuaLiKiz, the integration is performed not self-consistently as a simple averaging procedure to significantly speed up the calculation process.

Unresolvable Modes In the case of simultaneously low wavenumbers and values of $s - \alpha$, the stability of the system was found to be dominated by slab-type ITG-modes, peaked around ballooning angles θ being multiples of $\pm 2\pi$. Since the eigenfunctions used by QuaLiKiz are single Gaussians located around $\theta = 0$, slab-type ITG-modes cannot be resolved. Adopting the ansatz used by QuaLiKiz to include multiple Gaussians may resolve this issue, but is bound to cause additional difficulties.

Increased Disagreement for Low Wavenumbers Both the instability threshold gradients and the growth rates calculated with QuaLiKiz for low wavenumbers of $k_y = 0.1$ were found to disagree worse with GENE calculations in the regime of negative values of $s - \alpha$, i.e. small values of the magnetic shear, as compared to results obtained with QuaLiKiz using larger wavenumbers, i.e. $k_y = 0.3$ and $k_y = 0.5$. Here, contributions from small values of $k_x = sk_y\theta$ (cf. Eq. (2.18)) to the eigenfunction are weakened at larger ballooning angles as in the case of larger wavenumbers k_y , resulting in the appearance of additional peaks located at multiples of $\pm 2\pi$. Again, the eigenfunction ansatz used by QuaLiKiz is not suitable to resolve this phenomenon and would consequently require modifications to capture this behavior as well.

4.4 The JET Hybrid Scenario 75225

A validation of QuaLiKiz against GENE for experimentally relevant parameters in the regime of low values of the magnetic shear is performed using parameters from the JET hybrid scenario 75225^{39,40} at two radial positions. Using the results of the previous growth rate analysis, the behavior of QuaLiKiz in the JET case can be assessed in more detail. In previous investigations, cf. e.g. Refs. 14, 39, agreement between QuaLiKiz and GENE in the regime of low values of the magnetic shear was obtained only by neglecting the effect of α -stabilization, wherefore the behavior of QuaLiKiz and GENE is analyzed for both the case of experimental and negligible values of the α -parameter. The growth rates obtained as a function of the applied normalized ion temperature gradient R/L_{Ti} are illustrated in Fig. 4.5, whereas the corresponding eigenfunctions are presented in Fig. 4.6.

The inner location analyzed at a radial coordinate of $r/a = 0.42$ is characterized by a low magnetic shear of $s = 0.39$, with the α -parameter being $\alpha = 0.70$. Consequently, the parameters used are for the case of strong s - α -stabilization, explaining the low growth rates observed at this location. In the case of low wavenumbers of $k_y = 0.1$, the system is barely unstable, requiring an increase by 40% of the experimentally used ion temperature gradient to reach instability, according to GENE calculations. Whereas QuaLiKiz predicts a stable system throughout the range of normalized ion temperature gradients considered for the experimental value of the α -parameter, neglecting this parameter yields a better, yet rough approximation of the solution obtained by GENE. For increasing wavenumbers, the growth rates as calculated by GENE using $\alpha = 0.70$ are described significantly better by QuaLiKiz neglecting the influence of the α -parameter as opposed to the case where the experimentally obtained value of α is used for QuaLiKiz. In the later case,

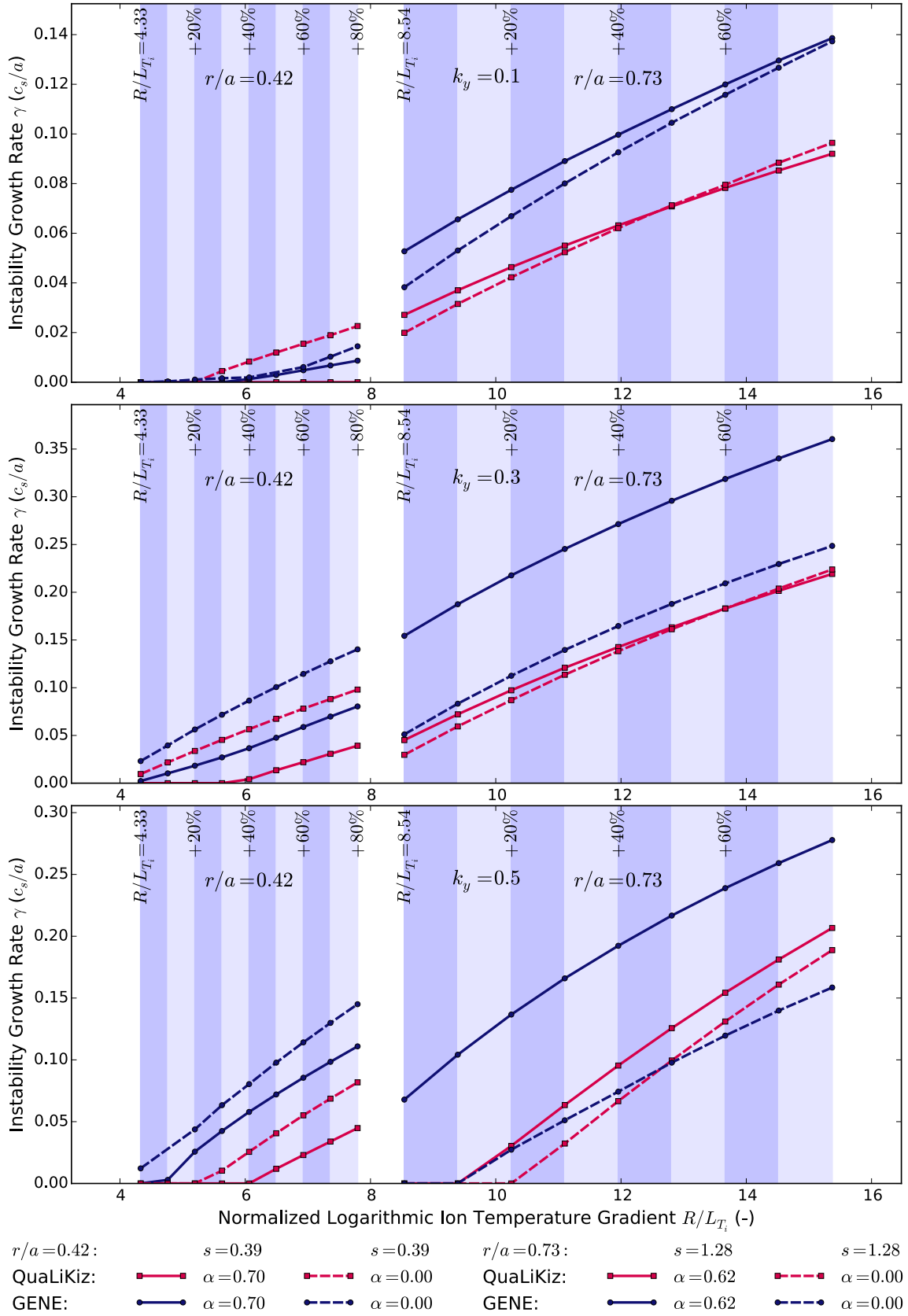


Fig. 4.5: Dependence of the instability growth rates of the JET hybrid scenario 75225 on the normalized ion temperature gradient R/L_{T_i} at the inner and outer location analyzed, calculated for three different wavenumbers using QuaLiKiz (red) and GENE with s - α -geometry (blue).

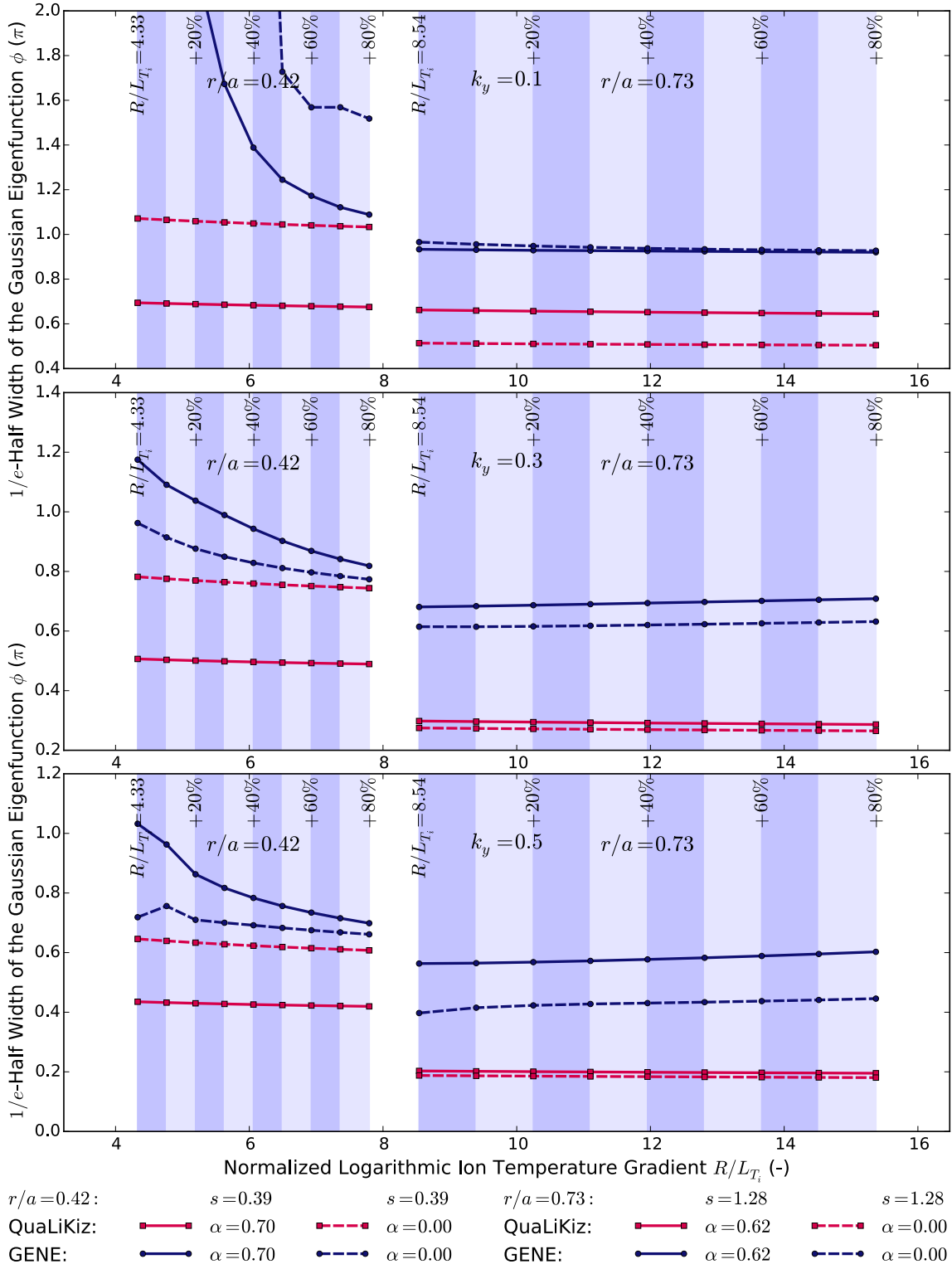


Fig. 4.6: Dependence of the 1/e-Half Width of the Gaussian Eigenfunctions of the JET hybrid scenario 75225 on the normalized ion temperature gradient R/L_{T_i} at the inner and outer location analyzed, calculated for three different wavenumbers using QuaLiKiz (red) and GENE with s - α -geometry (blue).

the threshold gradients calculated by QuaLiKiz are overestimated by 30 to 40% as compared to the ones calculated by GENE with $\alpha = 0.70$. However, by setting $\alpha = 0$ for QuaLiKiz, agreement of the threshold gradients is within 10%. Comparing this increase in agreement with the $1/e$ -width of the eigenfunctions, cf. Fig. 4.6, the eigenfunctions obtained with QuaLiKiz for a finite value of the α -parameter are significantly narrower than the eigenfunctions found by GENE. By neglecting the effect of α -stabilization, the width of the QuaLiKiz eigenfunctions approaches those of GENE.

The effect of increased agreement by setting $\alpha = 0$ can be explained by considering the change of the instability growth rate for varying values of $s - \alpha$ at a constant normalized ion temperature gradient R/L_{Ti} , cf. Fig. 4.2. For the given set of s and α , the parameters used at inner location of the JET case are located in the $s - \alpha$ -regime where an increase of the α -parameter stabilizes the system. Simultaneously, the effect of $s - \alpha$ -stabilization is severely overestimated by QuaLiKiz in this $s - \alpha$ -range, resulting in significantly lower growth rates as opposed to GENE. As consequently decreasing values of α have a destabilizing effect, neglecting the α -parameter in this case results in the growth rates found by QuaLiKiz approaching those obtained by GENE.

Although the growth rates obtained with QuaLiKiz for the outer location of the JET case, and thus for a larger value of the magnetic shear, were expected to agree well with results obtained by GENE for $\alpha = 0.62$, significant disagreement is observed, cf. Fig. 4.5. To obtain the growth rates as found by GENE at the experimental value of the ion temperature gradient, QuaLiKiz requires an increase of R/L_{Ti} by 30 to 60%. Consequently, the effect of $s - \alpha$ -stabilization is significantly overestimated at this comparatively high value of the magnetic shear of $s = 1.28$. Moreover, neglecting the effect of the α -parameter has only a minor influence on the growth rate obtained, even worsening the agreement with GENE using $\alpha = 0.62$. This phenomenon is also observed for the respective eigenfunctions, which are significantly narrower throughout the R/L_{Ti} -range considered than the solutions found by GENE. However, agreement in the growth rates calculated is significantly improved by setting $\alpha = 0$ for both QuaLiKiz and GENE, cf. Fig. 4.5.

Considering the values of s and α at the outer position of the JET scenario, this location is found to be located in the $s - \alpha$ -regime, where an increase of the α -parameter destabilizes the system, cf. Fig. 4.2. Consequently, the growth rates and eigenfunctions found with QuaLiKiz and GENE for negligible values of the α -parameter are respectively lower or narrower as opposed to the case of a finite α . Moreover, the phenomenon of growth rates as calculated by QuaLiKiz being virtually independent of α is observed in the same regime of $s - \alpha$, i.e. in the case of comparatively large values of the magnetic shear, cf. Fig. 4.2, whereas the GENE growth rates are found to decrease significantly by neglecting the effect of α -destabilization, cf. Fig. 4.5.

To further investigate the discrepancy of the growth rates between QuaLiKiz and GENE at the outer location, two additional cases with reduced normalized density gradients were analyzed to study the influence of trapped electron drive on the growth rate. In the first case, all density gradients were set to correspond to the electron density gradient of $R/L_{ne} = 3.24$, greatly reducing the large carbon impurity density gradient of $R/L_{nc} = 10.82$. However, no improved agreement as compared to the analysis using the original density gradients is observed, cf. Fig. 4.7. For the second case using $R/L_n = 1.0$, the agreement between QuaLiKiz and GENE improved slightly, eliminating trapped electron drive as reason for the discrepancy observed. As in the analysis of the JET hybrid scenario using the original density gradients, agreement between QuaLiKiz and GENE is significantly improved by neglecting the effect of α -destabilization. Moreover, the growth rates obtained with QuaLiKiz are again found to be virtually independent of the choice of the α -parameter, whereas the growth rates calculated by GENE are sensitive to a change in α .

As a result, even though the parameters used in the JET hybrid scenario are slightly different than those of the modified Cyclone base case, the behavior at both the inner and the outer location of the JET case analyzed is consistent with the observations made in the growth rate analysis of Sec. 4.1.2. Consequently, results obtained for the JET case are subjected to the same issues as discussed in Sec. 4.3 for the more general comparison, requiring the modifications of QuaLiKiz addressed for reliable use for these scenarios.

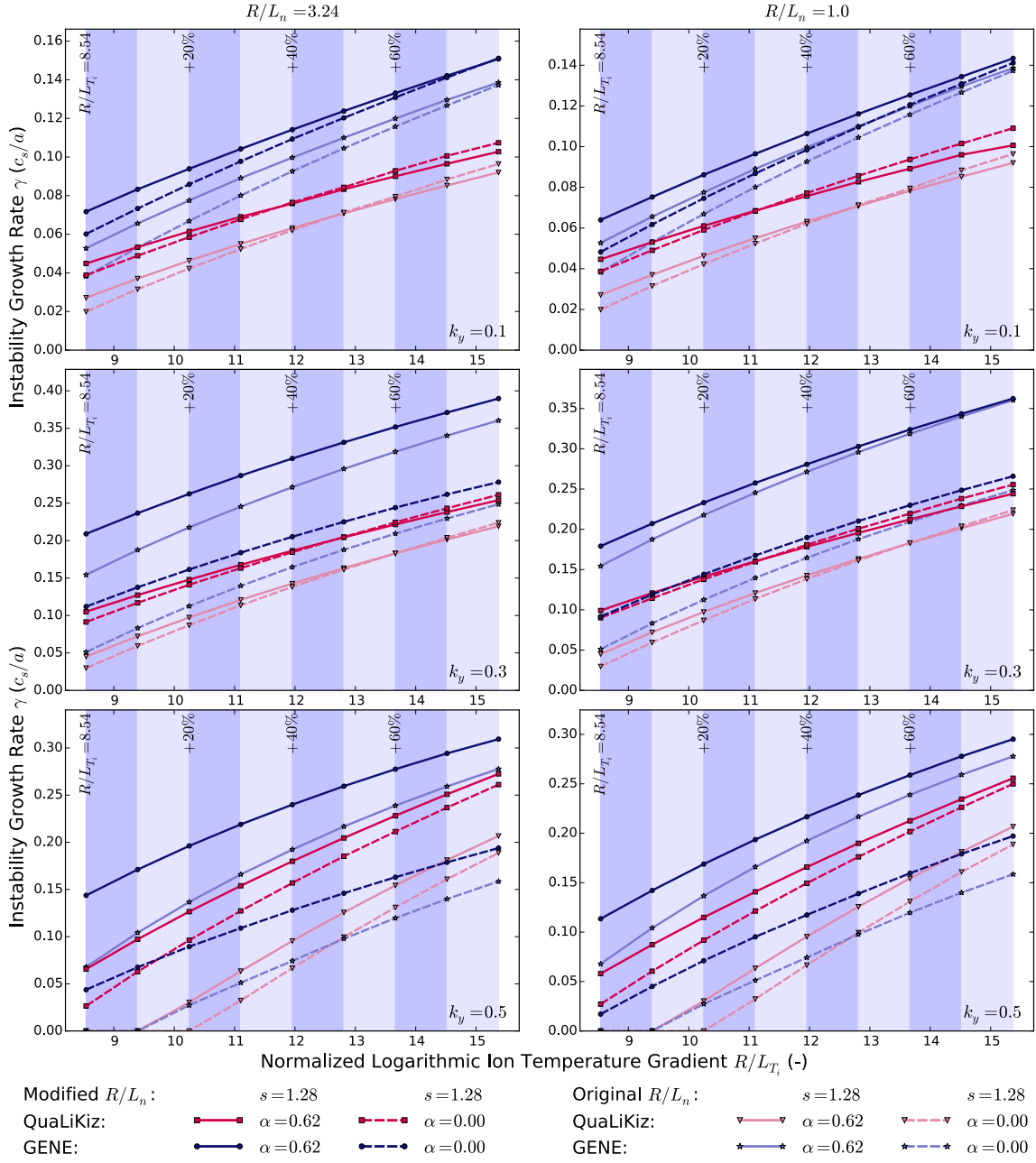


Fig. 4.7: Growth rates of the JET hybrid scenario 75225 for three values of k_y , where in the left column all density gradients were set to match the normalized electron density gradient $R/L_{n_e} = 3.24$, whereas in the right column all density gradients were reduced to $R/L_n = 1.0$. For comparison, the growth rates for the original density gradients are illustrated in pale colors. A slight improvement in agreement between QuaLiKiz and GENE is achieved for both choices of the α -parameter only for $R/L_n = 1.0$, eliminating trapped electron drive as reason for the discrepancy observed using the original density gradients.

5 Conclusion

In this work, the discrepancy of linear microstability calculations between the gyrokinetic codes QuaLiKiz and linear GENE observed previously¹³ has been investigated in the regime of low magnetic shear $s \in [-0.2, 1.5]$ and large values of the normalized pressure gradient $\alpha \in [0, 0.8]$ for electrostatically driven, toroidal ITG modes around the Cyclone base case. The analysis was carried out comparing instability threshold ion temperature gradients, instability growth rates at a constant value of the ion temperature gradient $R/L_{Ti} = 10$, as well as eigenfunctions of the electrostatic potential fluctuations. Furthermore, microstability calculations were performed for the JET hybrid scenario 75225 at two radial positions of low and high magnetic shear as to assess the validity of results obtained for practical parameters by comparison with the findings of the QuaLiKiz-GENE investigation around the Cyclone base case.

From gyrokinetic theory, particle drift and transit frequencies were found to be the relevant quantities influenced by changing values of the magnetic shear and the α -parameter, suppressing the development of instabilities in the regime of low values of $s - \alpha$. In the case of QuaLiKiz, this effect was found to be overestimated, resulting almost consistently in larger instability threshold gradients and lower instability growth rates as compared to linear GENE. For positive values of $s - \alpha$, the agreement between both codes was typically within 20%, whereas for negative values, deviations of the instability threshold gradients with respect to GENE calculations increased significantly. An increase of the differences in the growth rates obtained in this regime was found to be heavily dependent on the wavenumber k_y , such that using low values of $k_y = 0.1$ resulted in more severe disagreement below larger values of $s - \alpha \approx 0$ as compared to the case of wavenumbers $k_y = 0.3$ and $k_y = 0.5$, where increased disagreement was observed below $s - \alpha \approx -0.7$. Although being at least partially attributed to the choice of R/L_{Ti} , this effect illustrates increased discrepancy for lower wavenumbers due to additional components $k_x = sk_y\theta$ being weakened at larger ballooning angles. Furthermore, the appearance of slab-type ITG modes at simultaneously low values of the magnetic shear and the wavenumber is also responsible for increased disagreement in this regime, as these modes are unresolvable by QuaLiKiz due to the eigenfunction ansatz used. Additional deviations were observed at large values of both the magnetic shear and the wavenumber, where QuaLiKiz predicted growth rates and their corresponding eigenfunctions being virtually independent of the choice of the α -parameter in contrast to calculations by GENE. This phenomenon may be caused by an improper pitch angle integration of passing particles.

As the comparison of the effect of s - α -stabilization due to particle drift and transit frequencies requires identical implementations of the magnetic geometry in the codes used, the initial results obtained with GENE using shifted-circle-geometry were verified by additional scans in the regime of low magnetic shear performed with the more consistent Miller-geometry, using GENE and GKW. Contrary to expectations, noticeable differences between both geometries used were observed, with both codes using Miller-geometry predicting a larger effect of s - α -stabilization, thus agreeing better with QuaLiKiz calculations. For further assessment, analysis of the exact implementations of the different geometries used is necessary to assess the reason for the differences observed.

Several of the issues occurring in the comparison of QuaLiKiz and linear GENE around the Cyclone base case were also observed in the investigation of the JET hybrid scenario 75225. Due to overestimation of the effect of s - α -stabilization, growth rates at the experimental value of the ion temperature gradient as calculated by GENE using shifted-circle-geometry were only obtained with QuaLiKiz by using an ion temperature gradient increased by 30 to 60%. Alternatively, neglecting the effect of α -stabilization for QuaLiKiz calculations in the case of low values of the

magnetic shear also resulted in better agreement with GENE. Additionally, growth rates at the radial location corresponding to a large value of s were found to be independent of the choice of the α -parameter for all three wavenumbers analyzed, as also observed in the comparison of QuaLiKiz and GENE around the Cyclone base case.

Consequently, the issues found in this investigation have to be resolved to allow for a reliable use of QuaLiKiz in scenarios of low magnetic shear. Further work should thus focus on a review of the magnetic geometry implemented in GENE for both shifted-circle and Miller-geometry, on the exact comparison of the dependence of the drift frequency on the poloidal angle θ between QuaLiKiz and GENE, on a proper pitch angle integration, and on a reevaluation of the eigenfunction ansatz used.

Bibliography

- ¹ P.J. Mohr, B.N. Taylor and D.B. Newell. CODATA recommended values of the fundamental physical constants: 2010. *Rev. Mod. Phys.* **84**, 1527 (2012).
- ² D.J.C. MacKay. *Sustainable Energy - without the hot air*. UIT Cambridge, 2009.
- ³ IPCC. *Climate Change 2013: The Physical Science Basis. Contribution of Working Group I to the Fifth Assessment Report of the Intergovernmental Panel on Climate Change*. Cambridge University Press, 2013.
- ⁴ P. Moriarty and D. Honnery. What is the global potential for renewable energy? *Renew. Sustainable Energy Rev.* **16**, 244 (2012).
- ⁵ M. Höök and X. Tang. Depletion of fossil fuels and anthropogenic climate change - a review. *Energy Policy* **52**, 797 (2013).
- ⁶ P. K. Kaw and I. Bandyopadhyay. The Case for Fusion. In *Fusion Physics*. International Atomic Energy Agency, 2012.
- ⁷ J. P. Freidberg. *Plasma Physics and Fusion Energy*. Cambridge University Press, 2007.
- ⁸ K. Lackner et al. Equilibrium and Macroscopic Stability of Tokamaks. In *Fusion Physics*. International Atomic Energy Agency, 2012.
- ⁹ C. Bourdelle. *Turbulent Transport in Tokamak Plasmas: bridging theory and experiment*. Aix Marseille Université, 2015.
- ¹⁰ G.W. Hammett. Gyrokinetic theory and simulations of experiments. Orlando, Nov. 2007. APS Div. Plasma Physics.
- ¹¹ C. Bourdelle et al. Core turbulent transport in tokamak plasmas: bridging theory and experiment with QuaLiKiz. *Plasma Phys. Control. Fusion* **58**, 014036 (2016).
- ¹² C. Bourdelle et al. A new gyrokinetic quasilinear transport model applied to particle transport in tokamak plasmas. *Phys. Plasmas* **14**, 112501 (2007).
- ¹³ J. Citrin et al. Quasilinear transport modelling at low magnetic shear. *Phys. Plasmas* **19**, 062305 (2012).
- ¹⁴ J. Citrin. QuaLiKiz Update. Ahmedabad, Mar. 2016. 16th International Tokamak Physics Activity Transport & Confinement Topical Group Meeting.
- ¹⁵ C. Gormezano et al. Advanced tokamak scenario development at JET. *Fusion Sci. Technol.* **53**, 958 (2008).
- ¹⁶ W.A. Houlberg et al. Integrated modelling of the current profile in steady-state and hybrid ITER scenarios. *Nucl. Fusion* **45**, 1309 (2005).
- ¹⁷ X. Garbet et al. Physics of transport in tokamaks. *Plasma Phys. Controlled Fusion* **46**, B557 (2004).
- ¹⁸ X. Garbet. Drift wave turbulence: modeling and experimental aspects. Aix-en-Provence, July 2007. First ITER International Summer School.
- ¹⁹ Y. Sarazin. Turbulence and transport, 2013. University Lecture. Universités Paris VI & XI, Marseille I-II-II, Nancy I, Bordeaux I, INSTN, INPL, Ecole Polytechnique.

- ²⁰ A. Casati. *A quasi-linear gyrokinetic transport model for tokamak plasmas*. PhD thesis, Université de Provence (Aix-Marseille I), 2009.
- ²¹ C. Bourdelle. *Analyse de Stabilité de Plasmas de Tokamak*. PhD thesis, Université Joseph-Fourier (Grenoble-I), 2000.
- ²² R.E. LaQuey et al. Nonlinear saturation of the trapped-ion mode. *Phys. Rev. Lett.* **34**, 391 (1975).
- ²³ B.I. Cohen et al. Non-linear saturation of the dissipative trapped-ion mode by mode coupling. *Nucl. Fusion* **16**, 971 (1976).
- ²⁴ M. Romanelli, C. Bourdelle and W. Dorland. Effects of high density peaking and high collisionality on the stabilization of the electrostatic turbulence in the Frascati Tokamak Upgrade. *Phys. Plasmas* **11**, 3845 (2004).
- ²⁵ Ö.D. Gürcan. Turbulence in Fusion Plasmas, 2010. Talk. Laboratoire de Physique des Plasmas, Ecole Polytechnique, CNRS.
- ²⁶ J. Weiland. *Stability and Transport in Magnetic Confinement Systems*. Springer, 2012.
- ²⁷ X. Garbet et al. Gyrokinetic simulations of turbulent transport. *Nucl. Fusion* **50**, 043002 (2010).
- ²⁸ A.E. White et al. Measurements of the cross-phase angle between density and electron temperature fluctuations and comparison with gyrokinetic simulations. *Phys. Plasmas* **17**, 056103 (2010).
- ²⁹ R.J. Goldston and P.H. Rutherford. *Introduction to Plasma Physics*. Taylor & Francis Group, 2000.
- ³⁰ J. Candy, R.E. Waltz and M.N. Rosenbluth. Smoothness of turbulent transport across a minimum- q surface. *Phys. Plasmas* **11**, 1879 (2004).
- ³¹ J. Wesson. *Tokamaks*. Oxford University Press, 2004.
- ³² C. Bourdelle et al. Impact of the α parameter on the microstability of internal transport barriers. *Nucl. Fusion* **45**, 110 (2005).
- ³³ F. Jenko et al. Electron temperature gradient driven turbulence. *Phys. Plasmas* **7**, 1904 (2000).
- ³⁴ F. Jenko. Massively parallel Vlasov simulation of electromagnetic drift-wave turbulence. *Comput. Phys. Commun.* **125**, 196 (2000).
- ³⁵ F. Merz. *Gyrokinetic Simulation of Multimode Plasma Turbulence*. PhD thesis, Westfälische Wilhelms-Universität, Münster, 2008.
- ³⁶ G. Merlo et al. Linear multispecies gyrokinetic flux tube benchmarks in shaped tokamak plasmas. *Phys. Plasmas* **23**, 032104 (2016).
- ³⁷ A.M. Dimits et al. Comparisons and physics basis of tokamak transport models and turbulence simulations. *Phys. Plasmas* **7**, 969 (2000).
- ³⁸ R.L. Miller et al. Noncircular, finite aspect ratio, local equilibrium model. *Phys. Plasmas* **5**, 973 (1998).
- ³⁹ J. Citrin et al. Flux-driven multi-channel simulations with the quasilinear gyrokinetic transport model qualikiz. Leuven, Belgium, July 2016. 43rd European Physical Society Conference on Plasma Physics.
- ⁴⁰ J. Hobirk et al. Improved confinement in JET hybrid discharges. *Plasma Phys. Control. Fusion* **54**, 095001 (2012).
- ⁴¹ X. Lapillonne et al. Clarifications to the limitations of the s - α equilibrium model for gyrokinetic computations of turbulence. *Phys. Plasmas* **16**, 032308 (2009).